Size Effect on the Phase Stability of Nanostructures

Q. Jiang* and C. C. Yang

Key Laboratory of Automobile Materials (Jilin University), Ministry of Education, and Department of Materials Science and Engineering, Jilin University, Changchun 130022, China

Abstract: An extension of the classical thermodynamics to nanometer scale has been conducted to elucidate information regarding size dependence of phase transition functions and binary phase diagrams. The theoretical basis of the extension is Lindemann′s criterion for solid melting, Mott′s expression for vibrational melting entropy, and Shi′s model for size dependent melting temperature. These models are combined into a unified one without adjustable parameters for melting temperatures of nanocrystals. It is shown that the melting temperature of nanocrystals may drop or rise depending on interface conditions and dimensions. The model has been applied to size dependences of melting enthalpy and atomic cohesive energy, critical temperatures for glass transition, ferromagnetic transition, ferroelectric transition, superconductor transition and ferromagnetic-antiferromagnetic transition. Moreover, the above modeling has been utilized to determine the size-dependent continuous binary solution phase diagrams, bi-layer transition diagrams of metallic multilayers, and solid transition phase diagrams after modeling the transition entropy and atomic interaction energy functions of nanocrystals. Moreover, the model has been used to predict size dependence of diffusion activation energy and diffusion coefficient. These thermodynamic approachs have extended the capability of the classical thermodynamics to the thermodynamic phenomena in the nanometer regime.

Key Words: Thermodynamics; Phase transition; Nanocrystals; Phase diagram; Surface and interface.

1. INTRODUCTION

1.1. Scope

The contribution starts with a brief overview on essential thermodynamic properties of nanomaterials, especially on the phase transition. Deeper and consistent insight into the mechanism behind the observations and finding factors dominate the general trends of the size-induced property change, which are of fundamentally great importance for advancing technological applications. The typical phase transition, melting, is taken as the starting point to consider size dependence of phase transition. Lindemann′s criterion and several recent models for undercooling and superheating of nanocrystals under different interface conditions are comparatively discussed. In Section 2, a new approach for the melting temperature of nanocrystals is developed based on Lindemann′s criterion for the melting, Mott′s expression for the vibrational melting entropy, and Shi′s model for the size-dependent melting temperature with considerations of interface conditions and dimensions. In section 3, the model has been extended to predict size dependences of the cohesive energy, of glass transition temperature, ferromagnetic transition temperature, ferroelectric transition temperature, ferromagnetic-antiferromagnetic transition temperature, superconductor transition transition temperature, and solid structural transition temperature. In Section 4, three kinds of phase diagrams of nanocrystals are developed under the help of modelings of size dependences of melting entropy of crystals, of atomic interaction energy, of interface energy, and interface stress. Section 5 compares the current model predictions with available measurements and other theoretical results on the cohesive energy, the phase transition temperatures, the melting enthalpy, the phase diagrams, the diffusion activation energy, and diffusion coefficient of nanomaterials. Section 6 summarizes the main contributions and limitations of this work with suggestions for future directions in extending the developed knowledge and the associated approaches.

1.2. Overview

1.2.1. Thermodynamics of Macroscopic Systems

The classical thermodynamics on macroscopic systems has long been well established [1,2], which describes adequately macrscopic behaviors of bulk systems with changes of macroscopic parameters where the astrophysical objects and small systems at nanometer scale are excluded [3]. The basic thermodynamic relationship for a macroscopic system at equilibrium is [4],

$$dU = TdS - PdV \tag{1}$$

where U denotes the internal energy, T the absolute temperature, S the entropy, P the pressure, and V the volume. This equation connects incremental changes of internal energy, heat, and work.

In 1878, the monumental work of Gibbs first formulated a detailed thermodynamic phase equilibrium theory [1] where he transformed the previous complicated thermodynamics of cycles into the simpler thermodynamics of potentials and introduced chemical potentials [2]. Gibbs generalized Eq. (1) by allowing, explicitly, variations in the number of molecules N_i of the different components in a system [4]. As a result, Eq. (1) became $dU = TdS - PdV + \sum_i \mu_i dN_i$, or in a more general and modernized form,

$$dG = -SdT + VdP + \gamma dA + \sum_i \mu_i dN_i \tag{2}$$

where G and μ_i denote Gibbs free energy and the chemical potential of the component i, A denotes surface(interface) area and γ shows surface(interface) energy. Eq. (2) thus could treat various equilibria (chemical, phase, osmotic, surface, etc.) and examine many other topics, such as the equilibrium condition of a solid and a surrounding medium [2]. Eq. (2) is much easier to use than to understand although it is very simple mathematically. Although Eq. (2) has wide application ranges, it is essentially used to treat phase equilibrium and related phenomena, such as phase diagrams.

Later, the thermodynamic definitions of surface energy γ_{sv} and surface stress f_{sv} (subscripts s, l, v denote solid, liquid, and vapor, respectively, while two sybscripts together show the corresponding interface between the two states) are clarified to formulate surface thermodynamics [2]. This theme becomes more and more important due to the appearance of nanotechnology. However, due to the content limitation of this review, size dependences of surface thermodynamic functions are considered elsewhere.

Note that Eq. (2) with a statistic basis is only valid for materials being at least larger than submicron size while the parameter ″size″ in Eq. (2) is actually a constant of bulk. Since nanomaterials and nanotechnology go into the scientific and technical worlds now, extending the validity of thermodynamics into nanometer size range

*Address correspondence to this author at the Department of Materials Science and Engineering, Jilin University, Renmin Street, 5988, Changchun, 130022, China; Tel: +86-431-85095371; Fax: +86-431-85095876; E-mail: jiangq@jlu.edu.cn

1573-4137/08 $55.00+.00

thus becomes an urgent task. Namely, a further term or variant of size must be introduced into Eq. (2).

The above task can be reached by analyzing the size dependence of a typical known process of thermodynamic phase equilibriums, such as melting, which is so obvious in nature that even the ancient speculative physicists might expect to discuss it and have stimulated the development of classical thermodynamics in the nineteenth century [5]. Before the detailed consideration on size dependence, the most general bulk melting should be firstly introduced. In fact, the first and the second laws of thermodynamics expressed in Eqs. (1) and (2) can give a compact mathematical expression for melting thermodynamics with the bulk volume melting change V_m and the bulk melting enthalpy $H_m(\infty)$ where ∞ denotes the bulk size.

An alternative for studying the melting transition was carried out in 1910 by Lindemann for single component crystals with a kinetic consideration [6], which is much simpler than the usual phase equilibrium consideration based on the thermodynamics and will be used as the base of the present model. This quantitative model was based on Einstein′s explanation of the low-temperature specific heats of crystals $C_p(\infty)$ where the corresponding bulk characteristic Einstein temperature $\Theta_E(\infty)$ is proportional to the Einstein frequency $\nu_E(\infty)$, by $h\nu_E(\infty) = k\Theta_E(\infty)$ where h is Planck′s constant and k Boltzmann′s constant. This, as the first application of quantum theory to condensed matter physics, suggests that the atoms vibrate as quantized harmonic oscillators. At the melting for a given bulk crystal, the typical vibrational displacement $\sigma(\infty)$, or the root-mean-square (rms) average amplitude of atomic thermal vibration, should be some fixed fraction of the atomic or molecular diameter (the nearest atomic or molecular spacing) h, or $\sigma(\infty)/h = c = 1/2$. This implies that direct collisions between the atoms constituting the lattice would become possible, leading to the lattice demise. Lindemann′s argument accounts for anharmonicities in the problem but in a very generic fashion, through the existence of collisions. The theory relates the average thermal vibrational energy to T by the equipartition relation [5],

$$m_a\left[2\pi\nu_E(\infty)\right]^2\sigma(\infty)^2 = kT \tag{3}$$

where m_a is the atomic mass. Combining Eq. (3) and the above equation in the text, an expression in its modern form is present [5],

$$\Theta_D(\infty) = c\left[T_m(\infty)/\left(MV_s^{2/3}\right)\right]^{1/2} \tag{4}$$

where M is the atomic or molecular molar weight, V_s denotes the molar volume of solids, $T_m(\infty)$ is the bulk melting temperature.

Now it is known that c varies slightly with crystal structures: It is 0.13 for an fcc crystal and 0.18 for a bcc crystal [7]. This difference is partly due to the change of h, which depends on the coordination number (CN) of the specific structure [8]. h reduces with CN [9]. In order to eliminate or reduce this difference among distinct lattices or CNs, h can be determined not by the nearest atomic spacing, but by atomic volume that depends little on the lattice structure [8], and hence c is almost lattice-independent [10].

There are also other classic kinetic models for melting. Grüneisen correlates $T_m(\infty)$ with the reciprocal of the linear thermal expansion coefficient [11], while Born relates $T_m(\infty)$ to the absence of elastic resistance against shearing stress [12]. Both of the models share a similar physical nature of Lindemann′s one [13] and thus will not be further discussed.

Most of the melting experiments, such as calorimetric measurements, indicated that there are gradual changes of melting peak near T_m [5]. The broad melting transition peaks can be induced by dissolved impurities, by surfaces, and by polycrystallinity. The first produces a progressive lowering of T_m as the atomic concentrations in the liquid and solid change along the phase boundary. The second and the third bring a combination of surface/grain-boundary energy and size effects. Both contribute to the dropping of T_m. Since surface-melting is more evident, which is in nature a second order transition and occurs below T_m, this phenomenon has been specially studied [5]. The related model will be shown and discussed later.

However, the Lindamann′s model has its limitation. The model is based on harmonic forces, whereas melting must involve bond breaking or loosening [9,14]. The model, which depends on properties of the solid phase alone, cannot predict T_m convincingly. In fact, Lindemann did not intend to provide a "melting criterion" at all in his original paper, but rather pointed out the possibility to estimate the frequency of oscillators to support Einstein′s model for explaining C_p drop of solids at low temperatures [14].

Melting may be due to the intrinsic disorder created by thermal excitations, such as vibrational modes, point defects such as vacancies and interstitials, dislocations, and, in the case of molecular crystals, orientational defects [15,16]. Each type has a characteristic excitation energy dictating an exponential increase of the energy of solid with temperature. This leads also to lowering of T_m, where soild and liquid has the same G value. In addition, as we now understand, a proper analysis of dynamical melting should proceed with reference to process at the solid-liquid interface.

Despite the unsolved problems for the modeling of melting, Lindemann′s criterion has provided the most bases for predicting the melting behavior as it has been experimentally confirmed [10]. In the following, the criterion will be used to model the size dependence of the melting.

There are many models for other types of phase transition temperatures, such as magnetic transition temperatures [17]. The length limitation of this review however does not allow us to discuss them. Therefore, these phase transition models are omitted in this work.

1.2.2. Nanothermodynamics

One of the very basic concerns in mechanics, physics, chemistry and biomedical engineering of solids is the microstructure of a solid, which is determined by the chemical composition, the arrangement of the atoms and electrons (the atomic and electronic structures), and the size of a solid in one, two or three dimensions [18]. It is well-known that thermodynamic properties of nanometer-sized systems largely differ from those of single molecules as well as bulk materials. The reasons lie in the so-called specific and smooth size effects. The former is responsible for the existence of ″magic numbers″ and related irregular variation of properties in clusters, whereas the latter pertains to nanostructures in the size domain between clusters and bulk systems. Within this broad size range, mechanical, physical and chemical properties are often seen to change according to relatively simple scaling equations involving a power-law dependence on the system size due to the energy contributions of γ to the total G of the system with a high ratio of the surface volume to the entire volume $\chi = \Delta V/V$ [19]. These properties changes lead to, on one hand, an emerging interdisciplinary field involving solid state physics, chemistry, biology and materials science to synthesize materials and/or devices with new properties by controlling their microstructures on the atomic level. On the other hand, understanding the physical and chemical natures behind the new properties may provide guides for the design and fabrication of new materials and their possible industrial applications [18].

Among the above properties of solids, thermal stability of materials and devices are especially important, which is related to the corresponding T_m where $G_m = G_l - G_s = 0$ under a certain P. The melting, as a first order phase transition, requires $H_m \neq 0$ and $V_m \neq 0$. Since the value of $H_m << H_b$ with H_b being the vaporization enthalpy, the values of cohesive energy E_c and C_p of liquid and solid phases should be similar [5].

The melting entropy S_m and H_m are also essential thermodynamic parameters for melting. H_m is mainly produced by the internal energy change of atoms while S_m is induced by a structural change. Since $T_m = H_m/S_m$, only two among these three quantities are independent where the variation of S_m of different matters is much smaller than that of H_m and T_m, especially when the matters undergo atomic arrangement change without electronic transport. Note that all three quantities equal to zero or greater. When $S_m = H_m = 0$ at $T \neq 0$, the melting now deteriorates into a second order transition or a glass transition where there are no dramatic energy and structure changes.

As a variable for the melting thermodynamics, the size effect has only been studied in recent years due to the rapid progress in nanoscience and nanotechnology [5,14]. It is now known that $T_m(r)$ of metallic [20,21], semiconductor [22,23], and organic [24,25], nanocrystals are size-dependent where r denotes the size of the materials. While T_m of a free nanocrystal is known to decrease as r decreases [26], nanocrystals embedded in a matrix can melt below or above the corresponding $T_m(\infty)$ depending on interface structure between embedded nanocrystals and the matrix [27,28,29]. If the interfaces are coherent or semi-coherent, an enhancement of $T_m(r)$ occurs. Otherwise, there is a depression of $T_m(r)$ [30]. Some molecular dynamics (MD) simulations have also shown the same tendency [31,32,33]. To address these findings, the corresponding nanoscale thermodynamics, or nanothermodyanmics is needed where a larger χ value with decreasing r leads to increasing of G of both solid and liquid but in different speeds [34].

There are recently three kinds of fundamental approaches to open up the nanothermodynamics, which are based on fluctuations of temperature, the Tsallis′ entropy, and the Laplace-Young equation in small systems [3]. The first one is a generalized thermodynamic model dealing with nanosystems, as it starts with only the first law of thermodynamics and does not consider other thermodynamic relations [35,36]. The second one is on the basis of the Tsallis generalization of the ordinary Boltzmann-Gibbs thermostatistics by relaxing the additive properties of the thermodynamic quantities (the entropy, in particular) to include non-extensivity of nanosystems [37,38]. The last one considers the size-induced internal pressure $P_{in} = 2f_{sv}/r$, which may also be extended to a general case for the pressure effect on properties of bulk materials since any pressure source should have the same effect on materials properties [39]. These approaches developed from various perspectives can contribute significantly to understand properties of nanosystems. However, a consistent insight and a quantitative and unified model on nanothermodyanmics are still highly desirable. Since melting of nanocrystals has been widely studied, it will be firstly introduced to develop a basis of a unified model for nanothermodynamics on phase transitions.

1.2.3. Existing Models

$T_m(r)$ functions have been experimentally measured since 1954 by Takagi [26]. A linear relationship of $T_m(r) \sim 1/r$ is usually modeled, which is simply deduced in terms of χ being a function of dimension d. Both depression and enhancement of $T_m(r)$, which are named as undercooling and superheating where the thermodynamic melting points are lower or higher than the corresponding bulk one, have been found [13,27,29,30,40-45]. In addition, since 1940′s, surface melting below $T_m(\infty)$ with a thickness of several atomic layers of a solid is widely studied, which is a process proceeding under the condition of $\gamma_{sv} > \gamma_{sl}+\gamma_{lv}$ [6,47,48,49]. The physical nature of the surface melting is that although $\Delta G(T<T_m) = G_l(T<T_m)-G_s(T<T_m) > 0$, the condition of $\gamma_{sv} > \gamma_{sl}+\gamma_{lv}$ leads to formation of a liquid surface layer, which neutralizes the positive $\Delta G(T<T_m)$. This effect has naturally been enhanced due to the increase of χ [47,48].

The earliest thermodynamic consideration for $T_m(r)$ function was derived by Pawlow in 1909 where only the relative change from $T_m(\infty)$ was taken into account [49], which was even one year earlier than the modeling of $T_m(\infty)$ by Lindemann in 1910 [6] and much early than the experimental result in 1954 [26], which has the follow form,

$$T_m(r)/T_m(\infty) = 1 - 2V_s[\gamma_{sv} - \gamma_{lv}(\rho_s/\rho_l)^{2/3}]/(rH_m), \quad (5)$$

where ρ denotes mass density. For the most cubic metals [50,51],

$$\gamma_{sv} - \gamma_{lv} \approx \gamma_{sl}. \quad (6)$$

With $\rho_s \approx \rho_l$ and thus $(\rho_s/\rho_l)^{2/3} \approx 1$ and in terms of Eq. (6), Eq. (5) can be expressed as,

$$T_m(r)/T_m(\infty) \approx 1 - 2V_s\gamma_{sl}/(rH_m). \quad (7)$$

Actually, Eq. (7) is identical to the Gibbs-Thomson equation [52],

$$T_m(r)/T_m(\infty) = 1 - (1/r_1 + 1/r_2)V_s\gamma_{sl}/H_m \quad (8)$$

where r_1 and r_2 are principal radii of curvature of the interface that bound a solid. For a spherical particle, $1/r_1 = 1/r_2 = 1/r$, Eq. (8) = Eq. (7).

Before the most experimental results were present in 1990′s, Couchman and Jesser [53] have quantitatively modeled $T_m(r)$ in 1977,

$$T_m(r)/T_m(\infty) = 1 - [3(V_s + V_l)(\gamma_{sM} - \gamma_{lM})/2r - \Delta U]/H_m, \quad (9)$$

where subscript M denotes matrix, ΔU shows energy density difference between the nanocrystal and the nanoliquid. If ΔU is negligible, $T_m(r)$ can either higher or lower than $T_m(\infty)$, depending on the sign of $\gamma_{sM}-\gamma_{lM}$, which is closely related to the nature of the interface. Generally, $\gamma_{lM}-\gamma_{sM} = \gamma_{sl}\cos\theta$, where θ is the contact angle between a particle and the matrix ranged from 0° to 180° [54]. For a particle wetted by the matrix, $0^\circ \leq \theta < 90^\circ$ and $0 < \gamma_{lM}-\gamma_{sM} \leq \gamma_{sl}$ where the matrix/particle interface should be coherent or semi-coherent. Consequently, superheating happens and $T_m(r)$ increases with the decreasing of r. For a nanocrystal with $\theta \geq 90^\circ$, $\gamma_{lM}-\gamma_{sM} \leq 0$ and undercooling occurs.

Superheating has also been interpreted through various pressure effects, such as a capillary effect due to the decreasing r, the differential thermal expansion between the matrix and the nanocrystals, and the effect due to volume change during the melting [27]. However, these models underestimate experimental observations since they can only predict a very small superheating up to 6 K [27]. The reason is that they have only considered mechanical effects while the dominant chemical interfacial effect is neglected.

If the surface-melting phenomenon is taken into account, $T_m(r)$ function has different expressions [46,47,48,51],

$$T_m(r)/T_m(\infty) = 1 - 2V_s[\gamma_{sl}/(1-\delta/r) - \gamma_{lv}(1-\rho_s/\rho_l)]/(rH_m), \quad (10)$$

$$\frac{T_m(r)}{T_m(\infty)} = 1 - \frac{2V_s\gamma_{sl}[1-\exp(-\delta/\xi)]}{rH_m(1-\delta/r)} - \frac{V_s[(\gamma_{sv}-\gamma_{lv})-\gamma_{sl}(1-\delta/r)^2]\exp(-\delta/\xi)}{\xi H_m(1-\delta/r)^2}, \quad (11)$$

$$T_m(r)/T_m(\infty) = 1 - 2V_s\gamma_{sl}/[rH_m(1-\delta/r)], \quad (12)$$

where δ is layer thickness of surface liquid, ξ in Eq. (11) shows correlation length of solid/liquid interface. Note that when $\delta << r$, $\delta << \xi$ [46,47], $\rho_s \approx \rho_l$, and in terms of Eq. (6), Eqs. (10), (11), and (12) have essentially predicted the same trend as given by Eq. (7). This result implies that when r is large enough, the surface-melting phenomenon does not change the melting behavior of the nanocrystals although it indeed exists. However, when $r < 5$ nm ($\chi > 10\%$), Eqs. (10), (11), and (12) indicate a stronger melting point depression than Eq. (7) does. Note that once Eq. (7) comes into play, the surface-melting phenomenon disappears.

Another way to calculate $T_m(r)$ was made by Semenchenko [55] who has considered melting of a small solid particle embedded in the corresponding liquid, which has an exponential form,

$$T_m(r)/T_m(\infty) = \exp[-2V_s\gamma_{sl}/(rH_m)]. \quad (13)$$

Eq. (13) almost gives the same $T_m(r)$ value of Eqs. (10), (11), and (12) in the full size range of nanocrystals. As r increases, with a mathematical relation of $\exp(-x) \approx 1-x$ is valid where x is small, Eq. (13) ≈ Eq. (7). Since some variables in Eqs. (10), (11), and (12) come from fitting experimental results [46,47,50], Eq. (13) is more convenient to predict $T_m(r)$ when $r < 5$ nm with the same level of accuracy.

In the above equations, γ_{sl} value, as an important thermodynamic amount to determine $T_m(r)$ function, has been deduced recently according to Gibbs-Thomson equation [52],

$$\gamma_{sl} = 2hS_{vib}(\infty)H_m/(3V_sR) \quad (14)$$

where $S_{vib}(\infty)$ denotes vibrational melting entropy of bulk crystals and R is the ideal gas constant. Eq. (14) is capable of predicting γ_{sl} values quite accurately for element and compound crystals when the crystalline anisotropy is negligible [52,56]. Substituting Eq. (14) into Eq. (7),

$$T_m(r)/T_m(\infty) = 1 - 4hS_{vib}(\infty)/(3Rr) = 1 - (\alpha - 1)r_0/r, \quad (15)$$

where $\alpha = 2S_{vib}(\infty)/(3R)+1$ and $r_0 = 2h$. The exact meanings of them will be discussed later.

Note that although any surface reconstruction decreases γ_{sv}, such as roughing and surface melting, which seems to be neglected in Eq. (15), $S_{vib}(\infty)$ itself indeed has included the surface relaxation phenomenon. This is because $S_{vib}(\infty)$ value measured denotes the vibrational entropy difference at $T_m(\infty)$ between the solid and liquid where various surface relaxations of the solid have occurred. However, Eq. (15), or Eq. (7) still fails for correct description of $T_m(r)$ function of smaller nanocrystals where $\chi > 20\%$.

In Eq. (15), there is a size limit of $r = (\alpha-1)r_0$, at which $T_m(r) = 0$ K. If $r \le (\alpha-1)r_0$, $T_m(r) \le 0$, which is strictly forbidden in physics. As indicated above, when $r < 5\sim10\ r_0$, Eq. (7) or (15) is no longer valid. In contrast, Eqs. (10) (11), (12), and (13) can be applied to $(\alpha-1)r_0 < r < 5\sim10\ r_0$ due to the non-linear parts between $T_m(r)$ and $1/r$ in these equations.

It is interesting that although H_m function appears in above equations, it disappears in Eq. (15) since it is included in $S_{vib}(\infty)$. Thus, the detailed form of H_m is not of immediate concern.

Based on an analogy with the liquid-drop model [57,58] and empirical relations among $E_c(\infty)$, γ, and $T_m(\infty)$, $T_m(r)$ functions are determined as [59],

$$T_m(r)/T_m(\infty) = 1 - (c_2/r)(1 - \gamma_{Ms}/\gamma_{sv}) \quad (16)$$

where c_2 is a constant relating to atomic volume, $T_m(\infty)$ and γ_{sv}. Eq. (16) is very similar to Eq. (9) and could describe both undercooling and superheating of nanocrystals. For the case of undercooling, $\gamma_{Ms} = 0$. When superheating occurs, $\gamma_{Ms}/\gamma_{sv} > 1$.

Sun *et al.* [60] connects $T_m(r)$ function directly to the *CN*-imperfection effect on atomic cohesive energy of the lower coordinated atoms near the surface. It is suggested that the *CN*-imperfection causes the remaining bonds of the lower-coordinated atoms to contract spontaneously with an association of magnitude increase of the bond energy, i.e., bond-order-length-strength (BOLS) correlation [61], which contributes to E_c (the sum of bond energy ε over all coordinates of a specific atom with the coordination z, $E_c = zN_a\varepsilon/2$ with N_a being the Avogadro number), and hence to G that determines the thermodynamic behavior of a system. The thermal energy required to loosen the bonds of the specific atom is a portion of E_c. Thus, $T_m(r) \propto E_c(r)$, which leads to [62],

$$T_m(r)/T_m(\infty) = 1 + \sum_{i\le3}\beta_{ij}(z_{ib}c_i^{-m} - 1) \quad (17)$$

where β_{ij} is the volume or number ratio of the ith atomic layer to that of the entire crystal, $z_{ib} = z_i/z_b$ where z_i and z_b are the coordinates with and without *CN* imperfection, c_i shows *CN*-dependent reduction of bond length, and m is a parameter varying with the bond nature. The model indicates that the melting point change arises from the change of atomic cohesion of the under-coordinated atoms in the superfacial skins yet atoms in the core interior remain as they are in the bulk.

Moreover, the surface-phonon instability model [63,64] suggests that $T_m(r)$ is a function of two bulk parameters: $T_m(\infty)$ and the energy of formation of intrinsic defects. The shape effect on $T_m(r)$ for polyhedral nanocrystals, which is in nature also related to χ, is also considered and the corresponding shape factor is introduced [65,66].

In summary, all above models developed from various perspectives can contribute significantly to understanding the mechanism of $T_m(r)$ function. These models predict the same linear relationship between $T_m(r)$ and $1/r$ due to the surface effect when r is large enough. However, as $\chi > 10\%$, the dramatic drop of $T_m(r)$ is present because the energetic state of internal atoms also changes, which has been considered by Eqs. (10), (11), (12), and (13) in different approaches although their considerations are not directly related to energetic state of atoms, but χ. Since the superheating phenomenon was realized later than the undercooling one, the later models of Eqs. (9), (16), (17) attempted to determine both undercooling and superheating with also a similar linear relationship of $T_m(r) \sim 1/r$. The sign of the $1/r$ term is negative for undercooling but positive for superheating. Note that if the *CN* imperfection of the second surface layer is considered, Eq. (17) becomes a nonlinear function and could describe the melting behavior of smaller size of nanocrystals.

1.3. Challenge and Objectives

Although there are relatively extensive investigations on $T_m(r)$ as shown in the above, the studies for other nanothermodynamic functions are yet not so comprehensive, such as $S_m(r)$ and $H_m(r)$, which together with $T_m(r)$ function would compose the full thermodynamic functions of melting. Note that the solid-vapor transition enthalpy function $E_c(r)$ should be more directly related to the nature of the thermal stability of nanocrystals than $H_m(r)$ function [67], and should be considered.

Since the glass transition of nanoliquids and several magnetic transitions of nanocrystals, such as ferromagnetic, ferroelectric and superconductive transitions, have similar transition natures of the melting, the corresponding glass transition temperature $T_g(r)$ and the critical temperatures $T_c(r)$ may be determined by an extension of $T_m(r)$ function.

The above works usually are related to a single component (elements or compounds) while alloys are the most widely used in industry. To solve the nanothermodynamics problem in alloy systems, nanophase diagrams are necessary [68]. Since the nanophase equilibrium is metastable in nature and is difficult to measure, a theoretical work may be an alternative. In addition, metastable nanophases of a substance could not be exclusive where several metastable phases are present in different size ranges, which could be even absent in bulk [69]. Thus, the size-dependent phase diagrams also draw great interest of researchers and the related nanothermodynamic problems need to be solved [70].

Size dependences of kinetics, such as diffusion activation energy $E(r)$ and diffusion coefficient $D(r)$, are closely related to nanothermodynamics. It is well known that $E(r) < E(\infty)$ and thus $D(r) >> D(\infty)$ [71,72,73]. The potential of this phenomenon for industrial application is an evident drop of the working temperature for diffusion process. The theoretical understanding of this problem becomes more urgent due to not only the rapid developments in the industrial fields of Integrated Circuit (IC) and Micro Electronic Mechanical System (MEMS), but also recent progress in the nanotechnology, especially in pharmacy.

Based on the experimental observations, numerous models have been developed to understand mechanisms and changes of nanophase transitions. All these models developed from various perspectives can significantly improve our understanding of the mechanisms. However, it is often that a single phenomenon corresponds to numerous models. A unified model dealing with not one, but all related phenomena is thus useful. This unification certainly brings out comprehenion of interdependence of among different phase transitions.

The main objective of this contribution is to present a review firstly for the melting of nanocrystals and give a systematical analysis on both modeling considerations and experimental observations in order to discover the mechanism for the melting transition in a thermodynamic approach. This general model is extended into different fields and dealt with distinct phase transitions and phase diagrams. The physical relationship among these phase transitions is discussed. In nature, all transition temperature changes are determined by their size dependences of internal energies of phases where their change rates with size are different.

2. PRINCIPLE: ATOMIC VIBRATIONAL INSTABILITY

2.1. Mean Amplititude of Atomic Thermal Vibration of Nanocrystals

According to Shi′s model for $T_m(r)$, the mean-square displacement of a nanoparticle $\sigma^2(r)$ is shown as [21,74],

$$\sigma^2(r) = \sigma_{va}{}^2(r) + [\sigma_{sa}{}^2(r) - \sigma_{va}{}^2(r)]n_{sa}/n_{va} \quad (18)$$

where the subscripts *sa* and *va* denote atoms/molecules at the surface and located within the particle, respectively. $n_{sa}/n_{va} = \chi = (4\pi r^2 h/V)/[(4/3)\pi r^3/V\text{-}4\pi r^2 h/V] = r_0/(r\text{-}r_0)$ with $r_0 = 3h$ for a spherical or a quasi-spherical particle. Since both $\sigma_{va}{}^2(r)$ and $\sigma_{sa}{}^2(r)$ are larger than the corresponding $\sigma_{va}{}^2(\infty)$ and $\sigma_{sa}{}^2(\infty)$, it is assumed that $\sigma_{va}{}^2(r)/\sigma_{sa}{}^2(r) = \sigma_{sa}{}^2(\infty)/\sigma_{va}{}^2(\infty) = \alpha$ is size-independent although $\sigma_{sa}{}^2(r)$ and $\sigma_{va}{}^2(r)$ are size-dependent. Moreover, since the cooperative coupling between the surface and the interior atoms/molecules of small particles may be important, it is phenomenologically considered that the variation of $\sigma^2(r)$ is dependent on the value of $\sigma^2(r)$ itself. Thus, a change in σ^2 with χ can be given by $\sigma^2(\chi+d\chi)-\sigma^2(\chi)=(\alpha-1)\sigma^2(\chi)d\chi$ [21]. Integrating this equation yields,

$$\sigma^2(r)/\sigma^2(\infty) = \exp[(\alpha-1)x] = \exp\{(\alpha-1)/[(r/r_0)-1]\} \quad (19)$$

where r_0, at which all atoms/molecules are located on the surface, can be extended for different dimensions d with $d = 0$ for nanospheres, $d = 1$ for nanowires and $d = 2$ for thin films. For a nanosphere and a nanowire, r has the usual meaning of radius. For a thin film, r denotes its half thickness. r_0 is given by (1) $r_0 = 3h$ for $d = 0$ since $4\pi r_0{}^2 h = 4\pi r_0{}^3/3$; (2) $r_0 = 2h$ for $d = 1$ since $2\pi r_0 h = \pi r_0{}^2$; and (3) $r_0 = h$ for $d = 2$ since $2h = 2r_0$. Note that for disk-like nanoparticles, its quasi-dimension has been defined as $d = 1$ since its χ is between that of particles and that of thin films [75]. In short,

$$r_0 = c_1(3\text{-}d)h. \quad (20)$$

In Eq. (20), c_1 is added as an additional condition for different surface states. $c_1 = 1$ for nanocrystals with free surface where the potential of surface atoms of the nanocrystals differs from that of the interior of the nanocrystals. When the interface interaction between the nanocrystals and the corresponding substrate is weak, such as thin films deposited on inert substrates, the film/substrate interaction is weak van der Waals forces while the inner interactions within the thin films are strong chemical bonds, $c_1 = 1$ too. If this strength on the interface is compariable with that within films, c_1 varies somewhat [76]. When these are similar, which is equal to the case that one of the two surfaces of the films disappears and $c_1 = 1/2$ is thus got (the side surfaces of the thin films are neglected due to the low thickness). For more complicated interfaces, c_1 may be considered case by case between 1/2 and 1.

2.2. Solid-Liquid Transition

Since usually $T_m(r) > \Theta_D(\infty)$, the high temperature approximation can be utilized [21,74], $\sigma^2(r,T) = F(r)T$, where $F(r)$ is a size-dependent function. Thus, at any T, $\sigma^2(r,T)/\sigma^2(\infty,T) = F(r)/F(\infty)$. Moreover, when $T = T_m$, $F(r)/F(\infty) = \{\sigma^2[r,T_m(r)]/h^2\}/\{\sigma^2[\infty,T_m(\infty)]/h^2\}[T_m(\infty)/T_m(r)] = T_m(\infty)/T_m(r)$ in terms of Lindemann′s criterion if the size dependence of h is neglected. In summary [21],

$$T_m(r)/T_m(\infty) = \sigma^2(\infty)/\sigma^2(r) = \exp\{-(\alpha-1)/[(r/r_0)-1]\}. \quad (21)$$

In Eq. (21), if $\alpha > 1$, which is determined solely by $S_{vib}(\infty)$ [see Eq. (23)], $T_m(r)$ decreases with decreasing r; When $\alpha < 1$, which is related to the relative size of h and $T_m(\infty)$ between the nanocrystals and the matrix [see Eq. (25)], $T_m(r)$ increases with decreasing r.

In Eq. (21), the smallest size of crystals is assumed to be $2r_0$ where a half of atoms of a crystal is located on the surface with $\chi = 1$. $T_m(2r_0) = T_m(\infty)\exp(1\text{-}\alpha)$ where the both have almost the same short range order and the structure difference between crystal and liquid is little. As results, melting disappears. When $\alpha > 1$, $T_m(2r_0)$ is the lowest melting temperature and vise verse. Since $S_{vib}(\infty) > 0$, $\alpha \neq 1$ [see Eq. (23)] and thus $T_m(r) \neq T_m(\infty)$ for the undercooling case. For the superheating case, when $T_m(\infty)/T_M(\infty) = (h/h_M)^2$, $\alpha = 1$ [see Eq. (24)]. However, this is physically impossible since $T_m(\infty) \propto 1/h$ [8].

α in Eq. (21) has been determined by considering $S_{vib}(r)$ deduced by Mott′s expression for $S_{vib}(\infty)$ [10,77],

$$S_{vib}(r) = S_{vib}(\infty) - (3R/2)(\alpha-1)/[(r/r_0)-1]. \quad (22)$$

For a free-standing or a quasi-free-standing nanocrystal, $S_m(2r_0) = S_{vib}(2r_0) = 0$ is assumed for the smallest nanocrystal as stated above, which leads to,

$$\alpha = 2S_{vib}(\infty)/(3R) + 1. \quad (23)$$

For nanocrystals embedded in a matrix with coherent or semi-coherent interfaces, under the assumption that σ of the interfacial atoms of the nanocrystals has an algebraic average value between that of interior atoms of the nanocrystals and that of the matrix, α is determined as [78],

$$\alpha = \{[T_m(\infty)/T_M(\infty)](h_M/h)^2 + 1\}/2. \quad (24)$$

The surface melting as a continuous melting can be considered as a second-order transition [79]. $T_{sm}(r)$ function can be achieved from Eq. (21) when $S_{vib}(\infty)$ in Eq. (23) is substituted by $C_{pm}(\infty)$, which is the heat capacity difference between the liquid and the crystal at $T_m(\infty)$. The corresponding α value is shown as [79],

$$\alpha = [2C_{pm}(\infty)/(3R)] + 1. \quad (25)$$

Substituting Eqs. (23) or (24) or (25) into Eq. (21) in terms of Eq. (20), undercooling, superheating, and surface melting of nanocrystals can be quantitatively determined when the related materials

constants of h, $T_m(\infty)$, $S_{vib}(\infty)$, or $C_{pm}(\infty)$ are known. For elements and compounds, h, $T_m(\infty)$, and $C_{pm}(\infty)$ can be found from references while $S_{vib}(\infty)$ needs to be considered in details.

Since $S_m(\infty)$ consists, at least, of three components: configurational $S_{conf}(\infty)$, vibrational $S_{vib}(\infty)$ and electronic $S_{el}(\infty)$ [80], $S_m(\infty) = S_{vib}(\infty)+S_{conf}(\infty)+S_{el}(\infty)$ is assumed. $S_{conf}(\infty) = -R(y_A\ln y_A+y_B\ln y_B)$ [81], where y_A and y_B are the molar fractions of the crystals and vacancies, respectively, with an assumption that the melting of a crystal brings out solely formation of additional vacancies in the corresponding liquid where the structure of liquid remains a quasi-crystalline one. For the melting process, $y_A = 1/(1+\Delta V_m/V_s)$ and $y_B = 1-y_A$ where $\Delta V_m = V_l-V_s$. For metallic and organic crystals, the type of chemical connection does not vary during the melting [10]. Thus, $S_{el}(\infty) \approx 0$ [80], and $S_{vib}(\infty) = S_m(\infty)-S_{conf}(\infty)$, or

$$S_{vib}(\infty) = S_m(\infty) + R(y_A \ln y_A + y_B \ln y_B) \quad (26)$$

However, for semiconductor crystals and semi-metals, melting is accompanied by a semiconductor-to-metal transition and $S_{el}(\infty)$ strongly contributes $S_m(\infty)$. In this case, $S_{vib}(\infty)$ is determined by Mott′s equation in the following form [77,82],

$$S_{vib}(\infty) = (3R/2)\ln(\sigma_{cs}/\sigma_{cl}) = 3R\ln(\nu_{fs}/\nu_{fl}) \quad (27)$$

where σ_c and ν_f are the electronic conductivities and the vibrational frequencies, respectively. When above data are unavailable, the following equation can be roughly utilized [82,83],

$$S_{vib}(\infty) = S_m(\infty)-R. \quad (28)$$

Note that the contribution from $S_{conf}(\infty)$ in Eq. (28) has been neglected due to its relative small size.

The other two thermodynamic functions of melting besides $T_m(r)$ are $S_m(r)$ and $H_m(r)$. From the general thermodynamics,

$$H_m(r) = T_m(r)S_m(r). \quad (29)$$

If $S_m(r)$ has the same size-dependence of $S_{vib}(r)$, it reads in terms of Eq. (22) [10],

$$S_m(r) = S_m(\infty) - (3R/2)(\alpha-1)/[(r/r_0)-1]. \quad (30)$$

Thus, for free nanocrystals, in terms of Eqs. (23) and (30), there is [84],

$$S_m(r)/S_m(\infty) = 1-1/[(r/r_0)-1]. \quad (31)$$

Based on Eqs. (21) and (31), $H_m(r)$ function is determined,

$$\frac{H_m(r)}{H_m(\infty)} = \left[1-\frac{1}{(r/r_0)-1}\right]\exp\left[-\frac{2S_{vib}(\infty)}{3R}\frac{1}{(r/r_0)-1}\right]. \quad (32)$$

The physical nature for depression and enhancement of $T_m(r)$ may essentially be induced by different surface/interface conditions. For crystals with free-standing surface, the increase of the coherent energy of surface atoms of crystals is stronger than that of the corresponding liquid, which renders that $T_m(r)$ and $S_m(r)$ drop. For crystals embedded in a more stable matrix with coherent interfaces, the chemical bonds of the atoms on the coherent nanocrystals/matrix interface have more or less ionic characteristic, which leads to the enhancement of the bond strength on the interface and the lowering of G_s. Thus, $T_m(r)$ and $S_m(r)$ increase.

When $r/r_0 >$ 5-10, $\exp(-x) \approx 1-x$. Eq. (21) is simplified as Eq. (15) with $d = 1$. Since $T_m(r,d=0) < T_m(r,d=1) < T_m(r,d=2)$, Eq. (15) is a good approximation of Eq. (21) when the dimension effect on $T_m(r)$ is neglected. This is true when r is large enough.

The non-linear relationship between $T_m(r)$ and $1/r$ in Eq. (21) implies that besides χ, the interior atoms of nanocrystals have additional contribution on $T_m(r)$. This result shows good evidence that the macroscopic rules cannot simply be extended to microscopic size range with a linear relationship of $1/r$ when χ is large.

An emphasis should be carried out again that although the surface melting phenomena have not been directly considered in Eq. (21), it has been included in $S_{vib}(\infty)$ value since $S_{vib}(\infty)$ is experimentally determined with the existence of surface melting. Consequentially, Eq. (21) correlates to Eqs. (10), (11), and (12) well but without fitting parameters. Hence, Eq. (21) is more convenient to predict $T_m(r)$ function.

2.3. Solid-Vapor Transition: Cohesive Energy

As a natural consideration, $H_m(r)$ function of Eq. (32) should be applicable for $E_c(r)$ function if $S_{vib}(\infty)$ is substituted by the bulk evaporation entropy or the bulk liquid-vapor transition entropy $S_b = E_b/T_b$ with E_b and T_b being the bulk evaporation enthalpy and the evaporation temperature, respectively. Note that although the solid-vapor transition entropy should be used here, which is difficult to find in literatures, S_b as a first order approximation is acceptable since the structural difference between solid and liquid is much smaller than the correspondence with vapor. In light of this consideration, $E_c(r)$ function in terms of Eq. (32) is given as [85],

$$\frac{E_c(r)}{E_c(\infty)} = \left[1-\frac{1}{(r/r_0)-1}\right]\exp\left[-\frac{2S_b}{3R}\frac{1}{(r/r_0)-1}\right]. \quad (33)$$

In Eq. (33), $E_c(2r_0) = 0$ where the structure of the solid and the vapor is indistinguishable. Since a single atom/molecule cannot be identified whether it is in a solid or a vapor state, $2r_0 = h$, or, $r_0 = c_1h/4$. This equation differs from Eq. (20) with a factor of 1/12 where $d = 0$ has been taken, which is induced by the structural characteristic of vapor. To add the dimension effect, a similar consideration of Eq. (20) must be given, which leads to the following result,

$$r_0 = c_1(3-d)h/12. \quad (34)$$

This relationship brings out that Eq. (33) and Eq. (21) in nature show the same function at least for metals (their $S_{vib} \approx S_m$) since $S_b \approx 12S_m \approx 12 \sim 13R$ obtained by letting Eq. (34) = Eq. (20) or $2S_{vib}(\infty)h/(Rr) = S_bh/(6Rr)$. Thus $E_c \propto T_m$, as expected. Extending this relationship into the range of nanometer size, $E_c(r)/E_c(\infty) = T_m(r)/T_m(\infty)$. This relationship agrees with the general understanding [59,86].

3. OTHER PHASE TRANSITION TEMPERATURES OF NANOCRYSTALS

3.1. Glass Transition

According to Lindemann′s criterion for melting, as long as σ of atoms or molecules reaches a critical fraction of interatomic distance, a crystal will melt. During the transition, the viscosity of the crystal will drop sharply. In fact, this is also the transition characteristic of a glass transition. Since glasses and crystals as solids have the same structural feature of the short-range order, they should have the same vibrational characteristics at their melting temperatures of T_g and T_m. As a phenomenological observation, it is assumed that $\sigma_g^2(\infty) \approx \sigma^2(\infty)$ where the subscript g denotes at T_g although there is no rigorous justification for this [87,88,89]. Substituting this relationship into Eq. (21), namely letting $T_g(r)$, $T_g(\infty)$, $\sigma_g^2(r)$ and $\sigma_g^2(\infty)$ replace $T_m(r)$, $T_m(\infty)$, $\sigma^2(r)$ and $\sigma^2(\infty)$, it reads,

$$T_g(r)/T_g(\infty) = \sigma_g^2(\infty)/\sigma_g^2(r) = \exp\{-(\alpha-1)/[(r/r_0)-1]\}. \quad (35)$$

In Eq. (35), for free-standing films or those supported by a passivated substrate where there is a weak chemical film/substrate interaction of van der Waals force, the corresponding α (α_s) has been determined by [87],

$$\alpha_s = [2C_{pg}(\infty)/(3R)] + 1 \quad (36)$$

where $C_{pg}(\infty)$ is the heat-capacity difference between the bulk glass and the bulk liquid at $T_g(\infty)$. $\alpha_s > 1$ in Eq. (36) since $C_{pg}(\infty)$ is positive. Thus, $T_g(r)$ decreases as r decreases in light of Eq. (35).

For interfaces with hydrogen bonding, which is stronger than van der Waals bonding within the polymer, $\alpha_i = \sigma_i^2(r)/\sigma_v^2(r)$, where the subscript i denotes the interface. Since $\alpha_s = \sigma_s^2(r)/\sigma_v^2(r)$, $\alpha_i = \alpha_s\sigma_i^2(r)/\sigma_s^2(r)$. It is assumed that the bond strength is inversely proportional to σ^2, namely $\sigma_s^2(r) \propto 1/\varepsilon_s$ and $\sigma_i^2(r) \propto 1/\varepsilon_i$. Thus, $\sigma_i^2(r)/\sigma_s^2(r) = \varepsilon_s/\varepsilon_i$, or,

$$\alpha_i = \alpha_s\varepsilon_s/\varepsilon_i. \quad (37)$$

If $\varepsilon_s = \varepsilon_i$, this is possible when nanoparticles are embedded into a certain liquid, $\alpha_i = \alpha_s = 1$ and $T_g(r) = T_g(\infty)$. When ε_s and ε_i have comparable size, assuming that the total effect of both surfaces and the film/substrate interface on $T_g(r)$ is additive, there is,

$$\frac{T_g(r)}{T_g(\infty)} = \left\{\exp\left(-\frac{\alpha_s - 1}{(r/r_0) - 1}\right) + \exp\left(-\frac{\alpha_i - 1}{(r/r_0) - 1}\right)\right\}\Big/2. \quad (38)$$

To apply Eqs. (35) and (38) for polymer glasses, h in Eq. (20) is defined as the correlation length for intermolecular cooperative rearrangement, ξ_1, which is temperature-dependent [90,91]. It is known that the molecular weight of polymers M_w affects $T_g(r)$, possibly through ξ_1 [90,91,92,93]. However, when M_w is not special large, this effect is not evident and therefore is neglected for simplicity [87,92].

When a blend as a compatible system consists of two polymers where their interaction is essentially van der Waals force, the blend could be considered as a mixture and their properties may be additive. Let w be the weight fraction of the second polymer component, the corresponding $T_g(w,r)$ function of thin films may be determined by the Fox equation [94,95],

$$1/T_g(w,r) = (1-w)/T_g(0,r) + w/T_g(1,r). \quad (39)$$

Eq. (39) supplies an easy way to determine $T_g(w,r)$ function of polymer alloys when $T_g(0,r)$ and $T_g(1,r)$ are known from Eq. (35) or Eq. (38) where $w = 0$ or $w = 1$ is considered for components. Note that Eq. (39) for bulk is simply extended for thin films due to their interaction of two polymer components. This differs from metallic alloys with strong interactions among different atoms, which will be considered later.

3.2. Néel, Ferromagnetic, Ferroelectric, and Superconductive Phase Transition

Eq. (35) is also suitable for ferromagnetic-antiferromagnetic transition temperature or the Néel temperature $T_N(r)$,

$$T_N(r)/T_N(\infty) = \exp\{-(\alpha - 1)/[(r/r_0) - 1]\} \quad (40)$$

In Eq. (40), α (or α_s) can be obtained by Eq. (23) for nanocrystals with free surfaces. When there exists the film/substrate effect on α, the simplest case is that only the surface and interface coupling constants (J_s and J_i) differ from that within the film based on Ising model [96] while the effect induced by the exchange interface thickness is neglected. It is assumed that $J_i = J_s + J_{sub}$ as a first approximation where subscript *sub* denotes the corresponding substrate. Since $J \propto \varepsilon$ [17,97,98], in terms of Eq. (37), there is,

$$\alpha_i = \alpha_s J_s/J_i. \quad (41)$$

If the effects induced by surface and interface on $T_N(r)$ are additive, $T_N(r)/T_N(\infty)$ has the same form of Eq. (38) although their α values are different. Note that Eq. (38) is used for thin films. For nanoparticles and nanorods, the contribution of the substrate on $T_N(r)$ is neglected due to its little interface area and thus little interaction. In this case, Eq. (40) is directly used.

Although $T_c(r)$ of ferromagnetic, ferroelectric, and superconductor nanocrystals should have similar form of $T_N(r)$ function, an alternative for such kinds of transitions can also be direclty determined by introducing $E_c(r)$ function since in the final analysis all transitions come from change of their potential of atoms [99]. Based on the Ising premise and BOLS correlation mechanism, T_c is determined by the spin-spin exchange interaction $E_{exc}(T)$ [17,100]. The latter is the sum of a portion of E_c and the thermal vibration energy $E_v(T)$, e.g. $E_{exc}(T) = c_2E_c + E_v(T)$ with c_2 ($0 < c_2 < 1$) being a coefficient. According to the mean field approximation and Einstein's relation, $E_v(T) = kT$ [17,100]. At T_c, $E_{exc}(T) \approx 0$ and $E_v(T)$ required for disordering the exchange interaction is a portion of E_c at $T = 0$ [17,100]. Thus, $T_c \propto E_c$. If $T_c(r)$ is assumed to have the same size dependence of $E_c(r)$ as a first order approximation while $E_c(r)$ function has been obtained in Eq. (33),

$$T_c(r)/T_c(\infty) = E_c(r)/E_c(\infty). \quad (42)$$

4. PHASE DIAGRAM OF NANOCRYSTALS

4.1. Continuous Binary Solution Phase Diagram

The nanophase diagram is a very important theoretical tool for nanoalloys studies [101,102], which can be carried out by using the above models. Although the above consideration on polymer blends belongs to also the category of phase diagram, a little more complicated case, the continuous binary solution phase diagram of nanoalloys is considered here.

When the liquid and solid of a binary system are in equilibrium, the chemical potentials μ of component A in the both phases are equal, or

$$\mu_A^L = \mu_A^S \quad (43)$$

where the superscripts L and S denote liquid and solid, and the subscripts A and B denote the components (for the component B, there is the same equation but with subscript B). It is known that,

$$\mu_A^L = G_A^L + RT\ln a_A^L,$$

$$\mu_A^S = G_A^S + RT\ln a_A^S, \quad (44)$$

where a is the activity. In Eq. (44),

$$G_A^L - G_A^S = G_{mA} = H_{mA} - TS_{mA} = H_{mA} - TH_{mA}/T_{mA}. \quad (45)$$

Combining Eqs. (43), (44) and (45),

$$\ln(a_A^S/a_A^L) = H_{mA}(T_{mA} - T)/(T_{mA}RT). \quad (46)$$

Similarly, for component B,

$$\ln(a_B^S/a_B^L) = H_{mB}(T_{mB} - T)/(T_{mB}RT). \quad (47)$$

Let $a_A = \varphi_A x_A$ and $a_B = \varphi_B x_B$ with activity coefficient φ and atomic percentage x of a component where $x_A + x_B = 1$. For a regular solution, $\ln\varphi_A = (\Omega/RT)x_B^2$ and $\ln\varphi_B = (\Omega/RT)x_A^2$ in a quasi-chemical approach where Ω is atomic interaction energy [103]. Substituting the above relations into Eqs. (46) and (47),

$$H_{mB}(T_{mB} - T)/T_{mB} = \Omega^S(1 - x_B^S)^2 - \Omega^L(1 - x_B^L)^2 + RT\ln(x_B^S/x_B^L), \quad (48)$$

$$H_{mA}(T_{mA} - T)/T_{mA} = \Omega^S(x_B^S)^2 - \Omega^L(x_B^L)^2 + RT\ln[(1 - x_B^S)/(1 - x_B^L)]. \quad (49)$$

When T is certain, both x_B^L and x_B^S in a bulk phase diagram are unique and can be determined through Eqs. (48) and (49) when other quantities are known. Eqs. (48) and (49) can in return be util-

ized to determine Ω^S and Ω^L when T, x_B^L and x_B^S are available besides H_m and T_m. Since $\Omega^S(\infty)$ and $\Omega^L(\infty)$ are weak functions of composition for alloys whose components consisting of continious solution, as a first-order approximation, $\Omega^S(\infty)$ and $\Omega^L(\infty)$ will be determined at $T \approx (T_{mA}+T_{mB})/2$ with the corresponding x_B^L and x_B^S in the bulk phase diagrams.

The above discussion has introduced how to determine the solidus and liquidus curves in a phase diagram of binary regular continious solution and the method to determine $\Omega^S(\infty)$ and $\Omega^L(\infty)$ through the known bulk phase diagrams.

It is well known that $\Omega = N_a z[\varepsilon_{AB}-(\varepsilon_{AA}+\varepsilon_{BB})/2]$. All ε values, which are negative, decrease with reducing r [85,104]. If rates of decrease of ε are different, Ω is size-dependent. Since all thermodynamic quantities are roughly linear function of $1/r \propto \chi$ according to the general quantum chemistry consideration [105], Ω is assumed to have the same relationship. Because $H_m(2r_0) = 0$, $\Omega(r)$ should have the same limit and thus is assumed to have the following form,

$$\Omega(r)/\Omega(\infty) = 1 - 2r_0/r\,. \tag{50}$$

Since $2r_0 = 6h$ in terms of Eq. (20) where h is component-dependent, different components have distinct r_0 values. To avoid physically unreasonable negative $H_m(r)$ in terms of Eq. (32), a larger h value between two components will be taken to determine $2r_0$, which does not lead to evident error since the difference between two h values is usually smaller than 8% when the components could form continuous phase diagram. In light of Eq. (50), $\Omega^S(r)$ and $\Omega^L(r)$ have the same size-dependence and are composition-independent as a first order approximation. h value can also be more accurately determined by an algebra sum of h values of the both components. Now $\Omega(r)$ is a weak function of the component.

$T_m(r)$ and $H_m(r)$ of each component can be deduced in terms of Eqs. (21) and (32) where the corresponding $T_m(\infty)$ and $H_m(\infty)$ are known values. Taking $T_m(r)$, $H_m(r)$ and $\Omega(r)$ functions into Eqs. (48) and (49), binary continuous solution nanophase diagrams can be calculated.

4.2. Bi-phase Transition

Lindemann′s criterion in terms of Eq. (2) determines the phase transition temperature by a single phase instability consideration. When there exist several phases in a system, the above criterion fails. Thus, the thermodynamic method as the most general one is needed. Now we use this technique to treat the size dependence of phase transition and phase diagram.

It is known that metastable crystalline structures that differ from their bulk equilibrium phases can stabilize as r is reduced to the nanoscale regime although these changes in crystalline structures are often serendipitously discovered, and the corresponding understanding is rather limited [106,107].

The above mentioned case can be found in a generic B/A multilayer film where the phase stability of the film is a balance between volumetric and interfacial components of total free energy of a unit bi-layer consisting of one A layer, one B layer, and two B/A interfaces with change ΔG [108],

$$\Delta G = [\Delta\mu_A(1-V_B) + \Delta\mu_B V_B]\lambda + 2\Delta\gamma \tag{51}$$

where $\Delta\mu_i$ (i = A or B) denotes chemical potential difference per unit volume between the metastable and bulk phases, λ is the bi-layer thickness where $\lambda_A = (1-V_B)\lambda$ and $\lambda_B = V_B\lambda$ are the thickness of A and B, respectively, with V_B being the volume fraction of element B in the multilayer. Δγ is the corresponding difference of the interfacial energies between A and B with certain structures.

Phase stability zone of B/A multilayer system can be described by a bi-phase diagram with independent variables of V_B and 1/λ. Fig. (**1**) is such a bi-phase diagram where the both layers are thin in a size of several nanometers. When one is thinner than another, the thinner layer prefers to take a structure of the thicker layer to form coherent or semi-coherent interface, which results in the drop of the total free energy of the system since the corresponding interface energy is much lower.

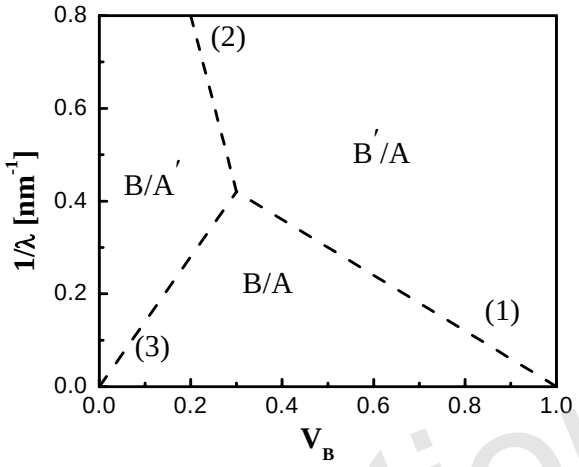

Fig. (1). The bi-phase diagram of B/A multilayers where the dashed lines are phase boundaries, the superscript ′ shows the element with a metastable structure.

As shown in Fig. (**1**), three bi-phase zones of B/A, B′/A and B/A′ appear. The zones meet at a triple point where all phases coexist. On the three lines $\Delta G = 0$. To determine these lines, three points and three line slopes are needed. Since the coordinates of two points located on lines (1) and (3) are (1,0) and (0,0), and the triple point is the common point, which adds an additional equilibrium condition, only three equations for the slopes of lines (1), (2) and (3) of m_1, m_2 and m_3 are needed. Let $\Delta G = 0$,

$$m_1 = -\Delta\mu_B/(2\Delta\gamma_1)\,,$$
$$m_2 = (\Delta\mu_B - \Delta\mu_A)/(2\Delta\gamma_2)\,,$$
$$m_3 = \Delta\mu_A/(2\Delta\gamma_3)\,, \tag{52}$$

where $\Delta\gamma_1$ and $\Delta\gamma_3$ denote the interface energy difference between B′/A and B/A interfaces, and that between B/A′ and B/A interfaces, respectively. $\Delta\gamma_2=\Delta\gamma_1-\Delta\gamma_3$.

Although Δμ values can be found in literatures, Δγ values are unknown, which need to be determined theoretically. Since a liquid may be regarded as a solid with such a high concentration of vacancies that these are in contact everywhere, γ_{ss} is considered to be approximately twice that of γ_{sl} [109], namely,

$$\gamma_{ss} \approx 2\gamma_{sl}\,. \tag{53}$$

An incoherent interface as above consists of different elements. As a first order approximation, the corresponding incoherent interface energy γ_{in} is assumed as a mean value of γ_{ss} of the both elements. In terms of Eqs. (14) and (53), there is,

$$\gamma_{in} \approx 4\overline{h}\overline{S}_{vib}(\infty)\overline{H}_m/(3\overline{V}_m R)\,, \tag{54}$$

where $\overline{h}$, $\overline{H}_m$, $\overline{S}_{vib}(\infty)$ and $\overline{V}_m$ are the mean values of corresponding elements consisting of interfaces.

When the interface concerned is coherent or semi-coherent, which corresponds to bilayers having the same structure and small interface misfit, the related interface energy γ_c is defined as,

$$\gamma_c = N_d u_d / A, \tag{55}$$

where $N_d = A/(l\eta)$ is the total dislocation number on the interface, A denotes the corresponding interface area, l is the length of the dislocation, $\eta/\overline{h} = h_A/(2|h_A - h_B|)$ is a half of the distance of two adjacent dislocations, u_d is the misfit dislocation energy of a single dislocation. The dislocation is assumed to be an edge one that is parallel to x-axis or y-axis, $u_d \approx \frac{g_A g_B b^2 l}{2\pi(g_A + g_B)(1+\nu)}[\ln\frac{\eta}{b} + 1]$ with neglecting of dislocation core energy [110] where $b = \overline{h}$ shows the Burgers vector, g and ν denote the shear modulus and the Poisson ratio, Substituting these quantities into Eq. (55), it reads,

$$\gamma_c = \frac{g_A g_B \overline{h} h_A/(2|h_A - h_B|)}{\pi(g_A + g_B)(1+\nu)}\left[\ln\frac{h_A}{2|h_A - h_B|} + 1\right]. \tag{56}$$

Note that according to the Goldschmidt premise for lattice contraction [111], atomic diameter contracts 3%, 4%, and 12% if *CN* of the atom reduces from 12 to 8, 6, and 4, respectively. Thus, when a body-centered cubic (bcc) phase transits to a hexagonal close packed (hcp) or face-centered cubic (fcc) phase, the corresponding h value contracts 3%, and vice versa. This lattice contraction has to be considered since h and thus γ_c values in Eq. (56) change considerably.

Let $\Delta\gamma = \gamma_{in} - \gamma_c$ and bear in mind the Goldschmidt premise for the h value, there is,

$$\Delta\gamma = 4\overline{h}\overline{S}_{vib}(\infty)\overline{H}_m/(3\overline{V}_m R) - \frac{g_A g_B \overline{h} h_A/(2|h_A - h_B|)}{\pi(g_A + g_B)(1+\nu)}\left[\ln\frac{h_A}{2|h_A - h_B|} + 1\right]. \tag{57}$$

When different structures with corresponding parameters are substituted into Eq. (57), $\Delta\gamma_1$ and $\Delta\gamma_3$, and thus $\Delta\gamma_2$ can be determined.

In Eq. (57), calculated $\Delta\gamma$ values account for only the structural component of the interfacial energy, where the related chemical component γ_{chem} is neglected. γ_{chem} is induced by consistance of different substances on the interface. If γ_{chem} for both are of a similar size, the neglect of γ_{chem} from the both hardly changes $\Delta\gamma$. In addition, γ_{chem} is associated with the bonding of atoms across the interface and is proportional to binary solution thermodynamic interaction energy $\omega = \Omega/z$ [112]. Since Ω is size-dependent and reduces to zero when λ is equal to about four atomic layers [113] and this size range is of interest in the current study, the discounting of the effect of γ_{chem} on the contribution of γ_{in} and γ_c does not lead to big errors.

4.3. Solid Phase Transition

Crystalline carbon is polymorphic in three structures of graphite (**G**), diamond (**D**) and fullerenes (**F**) [114]. The carbon bonding of **D** is sp^3 (tetrahedral) hybridization while that of **G** is sp^2 (trigonal) one. As results, **D** has a three-dimensional structure while **G** consists of two dimensional carbon layers stacked in an AB sequence. The layer interaction of **G** is linked by a weak van der Waals interaction produced by a delocalized π-orbital. **G** is the stable bulk allotrope of carbon at atmospheric pressures, and **G**→**D** transition occurs at high temperature and high pressure according to the equilibrium phase diagram of bulk carbon or when r is in nanometer size at low temperature and low pressure [114,115]. Furthermore, as r further decreases to 1 nm, **F** or carbon onions (**O**) could be the most stable form of carbon [116,117,118,119,120,121,122]. Note that **F** and **O**, which are not true graphitic phases, share many structural characteristics with **G**, e.g. sp^2 hybridization and six membered rings. Between **D** and **F** or **O**, an intermediary bucky diamond (**B**) phase with a **D**-like core and a **G**-like outer shell is often found.

The above transition phenomena could be thermodynamically determined by considering contributions of molar surface free energy G_s induced by γ_{sv}, molar elastic free energy G_e induced by surface stress f_s, and molar volume Gibbs free energy G_v, separately. Since they are functions of T and r, the free energy difference function between i and j phases $\Delta G^{i\to j}(T,r)$ can not be easilized to determine by distinguishing separately the effects of T and r. To realize this, the roughly definings that $\Delta G^{i\to j}(T,r)$ function is contributed by the sum of the temperature-dependent bulk value $\Delta G_v^{i\to j}(T)$, the size-dependent $\Delta G_s^{i\to j}(r)$, and the size-dependent $\Delta G_e^{i\to j}(r)$. Although two latter also have temperature effect on $\Delta G^{i\to j}(T,r)$, the effect is a higher order one since it has been partly countervailed since the related two phases have a similar temperature dependence. Thus, this error does not evidently affect the ultimate estimation about the phase stabilities of different nanocarbon polymorphs.

For a spherical and quasi-isotropic nanocrystal having a molar volume V_m under a constant pressure, $\Delta G^{i\to j}(T,r)$ function reads,

$$\Delta G^{i\to j}(T,r) = \Delta G_v^{i\to j}(T) + \Delta G_s^{i\to j}(r) + \Delta G_e^{i\to j}(r). \tag{58}$$

$\Delta G_s^{i\to j}(r)$ in Eq. (58) can be expressed as,

$$\Delta G_s^{i\to j} = A_m^j \gamma_{sv}^j - A_m^i \gamma_{sv}^i \tag{59}$$

where $A_m = 3V_m/r$ is the molar surface area. In Eq. (59), γ_{sv} is roughly defined to be isotropic. However, this approximation is wrong for strong anisotropic **G** where $\gamma_{svb}^G = 0.13$ J·m^{-2} and $\gamma_{svh}^G = 4.80$ J·m^{-2} with subscripts b and h denoting the basal and high-index planes, respectively [123]. Thus, γ_{sv}^G is defined as,

$$\gamma_{sv}^G = \frac{\gamma_{sb}^G A_b^G + \gamma_{sh}^G A_h^G}{A_b^G + A_h^G}, \tag{60}$$

where A with the corresponding subscript shows the corresponding area. The former is induced by van der Waals force while the latter is present due to the presence of the dangling bonds. The latest measured γ_{sv} values for single-walled and multi-walled nanotubes are 0.040 J·m^{-2} and 0.045 J·m^{-2} [124], which are about two orders smaller than γ_{sv}^D or γ_{svh}^G. Since the structures of **F** and **O** are similar to nanotubes, as a first order approximation, it is assumed that,

$$\gamma_{sv}^F \approx \gamma_{sv}^O \approx \gamma_{svb}^G \approx 0. \tag{61}$$

$\Delta G_e^{i\to j}(r)$ is expressed as,

$$\Delta G_e^{i\to j} = P_{in}^i V_m^i - P_{in}^j V_m^j. \tag{62}$$

In concerned nanocarbon structure, $V_m^F(r)$ is size-dependent and $V_m^F(r) = [V^F(r)/N^F]N_a$ where $V^F(r) = 4\pi r^3/3$ is the total volume of **F**, $N^F = 4\pi r^2/A_0$ is the corresponding number of carbon atoms with A_0 being surface atom density. Thus,

$$V_m^F(r) = N_a A_0 r/3. \tag{63}$$

As noted above, according to Laplace-Young equation [125],

$$P_{in} = 2 f_s / r \tag{64}$$

where f_s is determined by [126],

$$f_s = h[S_{vib}(\infty)H_m / 2\kappa V_m R]^{1/2}. \tag{65}$$

At equilibrium, $\Delta G^{i\to j}(T,r) = 0$. The corresponding critical size $r_c^{i\to j}(T)$ in terms of Eq. (58) is obtained as,

$$r_c^{i\to j}(T) = \frac{2(f_s^i V_m^i - f_s^j V_m^j) + 3(\gamma_s^j V_m^j - \gamma_s^i V_m^i)}{\Delta G_v^{i\to j}(T)}. \quad (66)$$

$\Delta G_v^{i\to j}(T)$ functions of **G**, **D**, **F** and **O** in Eq. (66) are separately determined one by one. $\Delta G_v^{G\to D}(T)$ functions of **G** and **D** can be found in terms of the bulk *T*-*P* phase diagram of carbon [114] and is expressed as,

$$\Delta G_v^{G\to D}(T) = P(T)\Delta V_m^{G\to D}, \quad (67)$$

where $\Delta V_m^{G\to D} = \Delta V_m^{D\to G}$ is approximately a temperature-independent constant [127], which implies that the dilatability difference between **G** and **D** within the considered temperature range has a secondary effect on $\Delta V_m^{G\to D}$ [128].

Since **F** can be considered as finite two-dimensional analogues of **G** without interlayer attraction and dangling edge bonds, $\Delta G_v^{D\to F}(T) \approx \Delta G_v^{D\to G}(T) + \Delta E_c^{G\to F}$ where $\Delta E_c^{G\to F}$ is the difference of cohesive energy between **G** and **F**. Note that a lot of isolated pentagon rule structures of **F** deviate from the sphere shape while related thermodynamic parameters are unavailable. Since C60 data can be found in literatures, as an example, C60 is used as the typical model molecule of **F** here. Other types of **F** can also be calculated when necessary parameters are known in a similar way. Note also that the corresponding formation entropy difference has been neglected as a first order approximation since the both phases have the same *CN*, i.e. the sp^2 bonding. Thus, substituting Eq. (67) into above $\Delta G_v^{D\to F}(T)$ expression, there is,

$$\Delta G_v^{D\to F}(T) = -P(T)\Delta V_m^{D\to G} + \Delta E_c^{G\to F}. \quad (68)$$

Since there are no interlayer attractions and dangling edge bonds for **F**, it has no molar van der Waals interlayer attraction E_v. If **O** is treated as nested F with E_v [120],

$$\Delta G_v^{F\to O}(T) = -E_v, \quad (69)$$

which can be supported by the fact that as the shell number of **O** goes up, its stability increases due to the appearance of E_v. Since present known experimental and theoretical results consider more about **D**→**O** transition [123,129], **D** is used as a standard state for comparison and $\Delta G_v^{D\to O}(T) = \Delta G_v^{D\to F}(T) + \Delta G_v^{F\to O}(T)$ function is thus considered in comparison with other known results. The $\Delta G_v^{D\to O}(T)$ function reads,

$$\Delta G_v^{D\to O}(T) = -P(T)\Delta V_m^{D\to G} + \Delta E_c^{G\to F} - E_v. \quad (70)$$

4.4. Diffusion Activity and Diffusion Coefficient

Although the title of this paper concerns with the thermodynamics, kinetics is often accompanied with thermodynamic phenomena and cannot be neglected. Since the energetic levels of atoms/molecules are size-dependent, the corresponding kinetics must be size-dependent.

The well-known Arrhenius dependence for self-diffusion or intrinsic diffusion coefficient of interdiffusion $D(r,T)$ has the following form [72],

$$D(r,T) = D_0(r)\exp[-E(r)/(RT)] \quad (71)$$

where $D_0(r)$ denotes a pre-exponential constant, $E(r)$ is the activation enthalpy.

To establish an $E(r)$ function, $D[r,T_m(r)] = D[\infty,T_m(\infty)]$ is assumed. This is because that at melting temperature, any solid state has the same vibrational characteristic in terms of Lindemann′s criterion. Thus, $D[r,T_m(r)] = D_0(r)\exp\{-E(r)/[RT_m(r)]\} = D_0(\infty)\exp\{-E(\infty)/[RT_m(\infty)]\}$ in terms of Eq. (71). According to a point defect mechanism, D_0 is proportional to $\exp(S_a/R)$ where S_a is the activation entropy. In light of a general thermodynamic relationship, $T[\partial S_a(r)/\partial T]_{Pin} = [\partial E(r)/\partial T]_{Pin}$ where $P_{in} = 2f_s/r$ denotes the pressure induced by surface stress. Thus, $S_a(r)$ is a function of $E(r)$. However, the change of $S_a(r)$ induced by vibrational frequency change due to the activation process is less than 5% even if r varies from bulk to 2-3 nm [130]. Thus, $E(r)$ is almost temperature-independent. Because the effect of the exponential term of $\exp[-E(r)/(RT)]$ on $D(r,T)$ is much stronger than $D_0(r)$, the latter is a weak function of r. As a first order approximation, $D_0(r) \approx D_0(\infty)$ is assumed (in the following, D_0 is used as abbreviation). Therefore,

$$E(r)/E(\infty) = T_m(r)/T_m(\infty), \quad (72)$$

where $T_m(r)/T_m(\infty)$ function has been deduced in Eq. (21). Substituting Eq. (21) into Eq. (72),

$$D(r,T) = D_0 \exp\left[\frac{-E(\infty)}{RT}\exp\left[\frac{-2S_{vib}(\infty)}{3R}\frac{1}{(r/r_0)-1}\right]\right]. \quad (73)$$

5. APPLICATIONS: CASE STUDIES

5.1. Cohesive Energy

Comparisons between model predictions in terms of Eq. (33) and experimental results for $E_c(r)$ functions of free Mo and W nanoparticles is shown in Fig. (**2**).

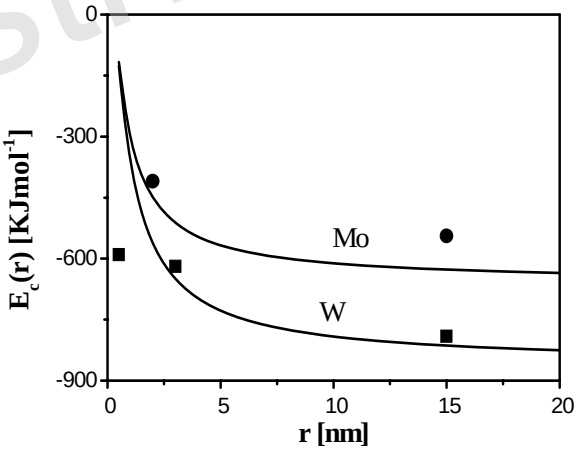

Fig. (2). $E_c(r)$ functions of Mo and W nanoparticles in terms of Eq. (33) shown as the solid lines and the symbols ● and ■ denote the corresponding experimental results of Mo and W, respectively [67]. For Mo, $E_c(\infty)$ = 659 KJ·mol^{-1} [131], S_b = 122.15 J·mol^{-1}·K^{-1} with E_b = 600 KJ·mol^{-1} and T_b = 4912 K [131], and h = 0.2745 nm [8]. For W, $E_c(\infty)$ = 860 KJ·mol^{-1} [131], S_b = 137.27 J·mol^{-1}·K^{-1} with E_b = 800 KJ·mol^{-1} and T_b = 5828 K [131], and h = 0.2741 nm [8].

As shown in Fig. (**2**), except $E_c(r = 0.5\text{ nm})$ value of W nanoparticles, Eq. (33) is consistent with the experimental observations. $E_c(r)$ increases with a drop in size, which reflects the instability of nanocrystals in comparison with the corresponding bulk ones due to the increase of χ and thus higher energetic state on average [85]. When r < 1-1.5 nm where the particles consist of only several ten to hundred atoms, a cluster structure is formed, which differs from the corresponding bulk structure, while Eq. (33) is valid only when the particle has the same structure of the bulk. This is the reason why the experimental $E_c(r = 0.5\text{ nm})$ value of W nanoparticles differs from the model prediction of Eq. (33).

5.2. Phase Transition Temperature

5.2.1. Melting Temperature

Fig. (**3**) shows $T_m(r)$ functions of Au and Ag with free-standing or quasi-free-standing surfaces based on Eq. (21) and the corresponding experimental results. As shown in Fig. (**3**), the model predictions are in good agreements with the both experimental and computer simulation evidences where dimension difference could also lead to distinct drops of $T_m(r)$. This is because at the same r, different d values have different χ.

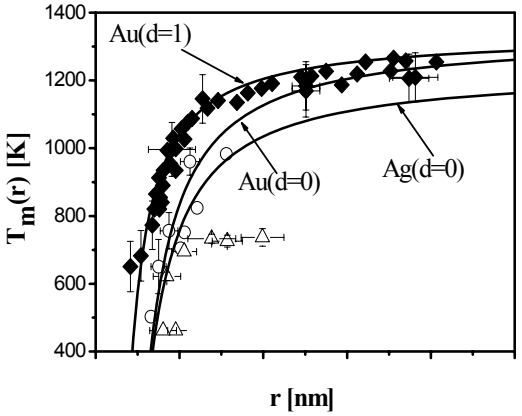

Fig. (3). $T_m(r)$ functions of noble metals nanocrystals in terms of Eqs. (20), (21) and (23) shown as the solid lines. For Au, $T_m(\infty)$ = 1337.33 K [131], $S_{vib}(\infty)$ = 7.74 J·mol^{-1}·K^{-1} in terms of Eq. (26) where $\Delta V_m/V_s$ = 5.1% [112] and $S_m(\infty)$ = 9.35 J·mol^{-1}·K^{-1} determined by $S_m(\infty) = H_m(\infty)/T_m(\infty)$ with $H_m(\infty)$ = 12.5 KJ·mol^{-1} [131], and h = 0.2884 nm [8]. The symbols ♦, O denote experimental and computer simulation results with d = 1 and d = 0, respectively [133]. For Ag, $T_m(\infty)$ = 1234.93 K [131], $S_{vib}(\infty)$ = 7.98 J·mol^{-1}·K^{-1} where $\Delta V_m/V_s$ = 3.3% [132] and $S_m(\infty)$ = 9.15 J·mol^{-1}·K^{-1} with $H_m(\infty)$ = 11.3 KJ·mol^{-1} [131], and h = 0.2889 nm [8]. The symbol Δ denotes experimental results with d = 0 [133].

Fig. (**4**) presents $T_m(r)$ and $T_{sm}(r)$ of semimetal In nanocrystals in different dimensions and different surroundings. $T_m(r)$ is indeed a function of d especially when r is small. Eq. (15) is thus a good approximation of Eq. (21) for mesoscopic particles of which $r > 5\text{-}10r_0$ and contributions from the interior atoms and from d are no longer prominent. In addition, according to Eq. (24), α decreases as

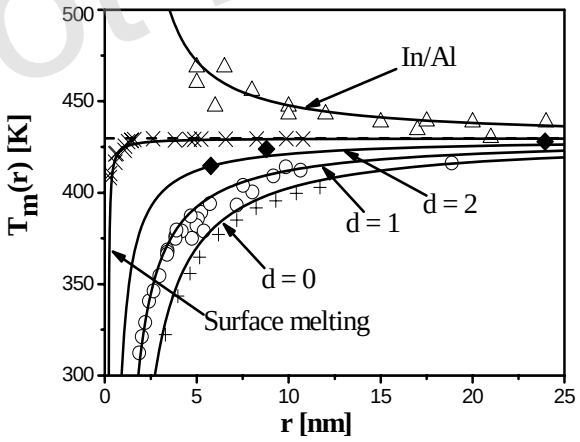

Fig. (4). $T_m(r)$ and $T_{sm}(r)$ functions of semi-metal In nanocrystals in terms of Eqs. (20), (21), (23), (24), and (25) shown as the solid lines. The dashed line presents $T_m(\infty)$ = 429.75 K [131]. For In, $S_{vib}(\infty)$ = 6.58 J·mol^{-1}·K^{-1} in terms of Eq.(26) where $\Delta V_m/V_s$ = 2.7% [132] and $S_m(\infty)$ = 7.59 J·mol^{-1}·K^{-1} with $H_m(\infty)$ = 3.26 KJ·mol^{-1} [131], h = 0.3684 nm [8], and $C_{pm}(\infty)$ = 0.707 J·mol^{-1}·K^{-1} [136]. For Al, $T_M(\infty)$ = 933.47 K [131] and h_M = 0.3164 nm [8]. The symbols ♦, O, and + denote experimental results with d = 2, d =1, and d = 0 for In nanocrystals with free surface or deposited on inert substrates [84]. The Symbol Δ and × show experimental results for the In/Al system and for the surface melting, respectively [84].

$T_M(\infty)/T_m(\infty)$ and h/h_M increases, both are essential and determine the superheating tendency of nanocrystals [78,134,135]. Note also that the size dependence of $T_{sm}(r)$ function is evidently weaker than that of $T_m(r)$ function even its r_0 is only a half of $T_m(r)$. This difference is induced by the fact that $S_m(\infty)/C_{pm}(\infty) \approx 11$, which implies that the driving force for the surface melting is much smaller than that for the melting [82].

$T_m(r)$ functions of molecular nanocrystals are shown in Fig. (**5**). Since the chemical bond among molecules is van der Waals type, all thermodynamic amounts of melting, namely $T_m(\infty)$, $S_m(\infty)$ and $H_m(\infty)$, are smaller than those of metallic, ionic and covalent bond nature. Thus, the corresponding dropping tendency of $T_m(r)$ is weak, which reacts through $S_{vib}(\infty)$ value in Eq. (21) and is introduced from Eq. (23). Thus, Eq. (21) can distinguish and describe $T_m(r)$ functions of all chemical combinations in a unique equation.

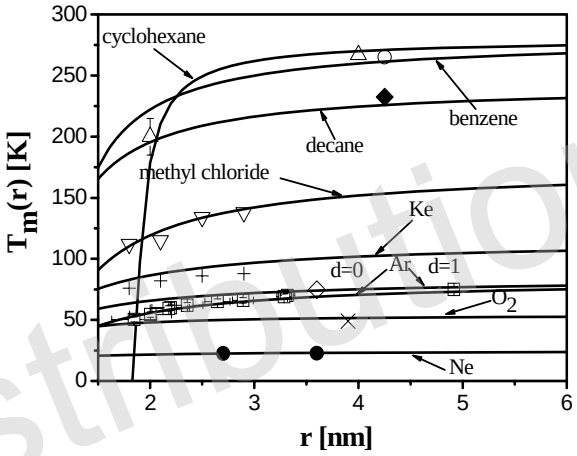

Fig. (5). $T_m(r)$ functions of cyclohexane, benzene, decane, methyl chloride, krypton (Ke), argon (Ar), oxygen (O_2) and neon (Ne) nanocrystals in terms of Eqs. (20), (21) and (23) shown as the solid lines. Necessary parameters and experimental data are all cited from the reference [137]. For cyclohexane, $T_m(\infty)$ = 279.82 K, $S_{vib}(\infty) \approx S_m(\infty)$ = 0.5311 J·g-atom^{-1}·K^{-1}, and h = 0.6088 nm. The symbol Δ denotes experimental and computer simulation results for porous spherosils with d = 0. For benzene, $T_m(\infty)$ = 280.8 K, $S_{vib}(\infty)$ = 2.842 J·g-atom^{-1}·K^{-1}, and h = 0.5066 nm. The symbol O denotes the experimental result in a single cylindrical pore with d = 1. For decane, $T_m(\infty)$ = 243.3 K, $S_{vib}(\infty)$ = 3.693 J·g-atom^{-1}·K^{-1}, and h = 0.425 nm. The symbol ♦ denotes the experimental result in a single cylindrical pore with d = 1. For methyl chloride, $T_m(\infty)$ = 175.6 K, $S_{vib}(\infty)$ = 7.317 J·g-atom^{-1}·K^{-1}, and h = 0.4141 nm. The symbol ∇ denotes the experimental result in a single cylindrical pore with d = 1. For Ke, $T_m(\infty)$ = 116.0 K, $S_{vib}(\infty)$ = 14.14 J·g-atom^{-1}·K^{-1}, and h = 0.206 nm. The symbol + denotes experimental results for nanowires with d = 1. For O_2, $T_m(\infty)$ = 54.4 K, $S_{vib}(\infty)$ = 4.073 J·g-atom^{-1}·K^{-1}, and h = 0.278 nm. The symbol × denotes experimental results for nanowires with d = 1. For Ne, $T_m(\infty)$ = 24.6 K, $S_{vib}(\infty)$ = 13.54 J·g-atom^{-1}·K^{-1}, and h = 0.102 nm. The symbol • denotes experimental results for nanowires with d = 1. For Ar, $T_m(\infty)$ = 83.81 K, $S_{vib}(\infty)$ = 14.18 J·g-atom^{-1}·K^{-1}, and h = 0.176 nm. The symbol □ denotes computer simulation results for nanoparticles with d = 0 and the symbol ◊ denotes experimental results for nanowires with d = 1.

Fig. (**6**) presents $T_m(r)$ function of H_2O embedded in MCM-41 in terms of Eq. (21). The value of α is different from the above since the interaction between surface molecules and the molecules on the pore wall must be considered.

As shown in the above, our model can predict $T_m(r)$ functions of low-dimensional crystals with different chemical bonds, different dimensions, and different surface or interface conditions since it covers all essential considerations of early models.

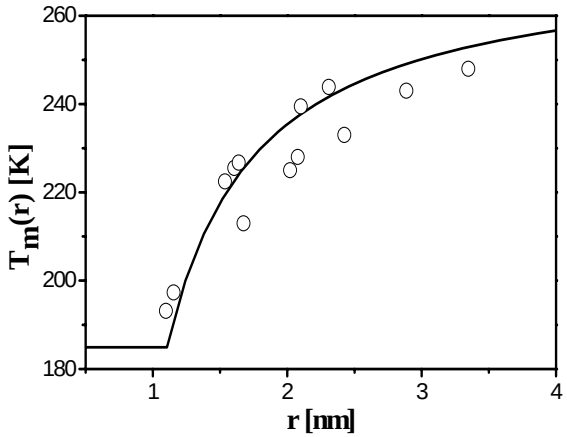

Fig. (6). $T_m(r)$ functions of nano-ice embedded in MCM-41 in terms of Eqs. (20), (21) and (23) shown as the solid lines. Necessary parameters and experimenta data are all cited from the reference [138]. For H_2O, $T_m(\infty)$ = 273.15 K, $S_{vib}(\infty) \approx S_m(\infty)$ = 7.37 Jg-atom^{-1}K^{-1}, $\alpha = [2S_{vib}(\infty)/(3R)+1](1-\beta)$ = 1.39 with β = 12.7% denoting a ratio of the surface molecules that interact with the molecules on the pore wall to the total number of surface ice molecules. The symbol O denotes the experimental results with d = 1 since the morphology of MCM-41 is cylindrical.

5.2.2. Glass Transition Temperature

Fig. (**7**) compares $T_g(r)$ function of polystyrene (PS) films with different surface conditions. As shown in Fig. (**7**), when the molecular force at the interface (surface) is stronger than that within the film, a superheating is present. In an opposite case, an undercooling occurs. Note again that the size dependence of $T_g(r)$ is much weaker since the glass transition is a second order transition where $C_{pg}(\infty)$ value in a size about (1/4-1/5)R in Eq. (36) is much smaller than the usual $S_{vib}(\infty)$ value of about R.

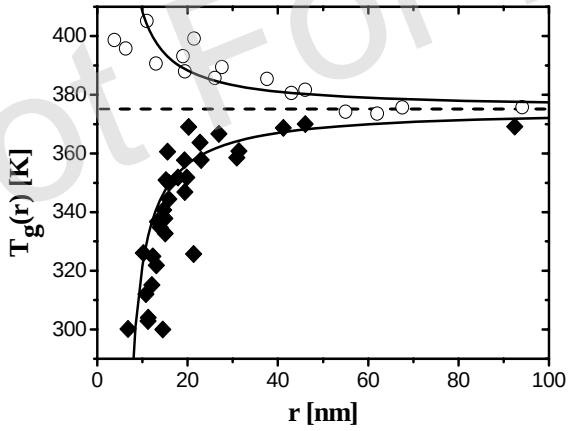

Fig. (7). $T_g(r)$ function of free-standing polystyrene (PS) films and PS films supported by Si substrate with hydrogen bonding in terms of Eqs. (35), (36), (38) and (20). The dashed line denotes $T_g(\infty)$ of PS. For free-standing PS films, d = 2, α_s = 1.154 determined by Eq. (36) where $C_{pg}(\infty)$ = 30.7 J·mol^{-1}·K^{-1} = 1.919 J·g-atom^{-1}·K^{-1} [87], $T_g(\infty)$ = 375.15 K [139], $r_0 = \xi_1$ = 5 nm with c_1 = 1 in terms of Eq. (20) where $\xi_1 = \xi_1[T<T_g(\infty)]$ = 5 nm [91], which is used to substitute h for polymers. The symbol ♦ shows the experimental results [76]. For PS films supported by Si substrate with hydrogen bonding, ε_i = 4.5 kcal·mol^{-1} is the mean hydrogen bonding strength of 4-5 kcal·mol^{-1} [140], ε_s = 1.5 kcal·mol^{-1} shows the mean van der Waals force of 1-2 kcal·mol^{-1} [140], Thus, α_i = 0.3885 in terms of Eq. (37). $r_0 = \xi_1$ = 2.5 nm with c_1 = 1 in light of Eq. (20) where $\xi_1 = \xi_1[T_g(\infty)]$ = 2.5 nm [91]. The symbol O denotes the experimental evidences [76].

Fig. (**8**) presents $T_g(w,r)$ function of poly(2,6-dimethyl-1,4-phenylene oxide)/polystyrene (PPO/PS) blended films supported by a passivated Si substrate. good correspondences among the model predictions, experimental results, and computer simulation results are shown where $T_g(w,r)$ decreases as r decreases and $T_g(w,r)$ decreases as w increases since $T_g(1,\infty) < T_g(0,\infty)$. The successful application of Eq. (39) implies that the chemical interaction between polymer films is weak. Thus, their interaction nature of van der Waals force is not necessary to be specially considered. The properties of the composite can be simply determined by an algebra sum of the components.

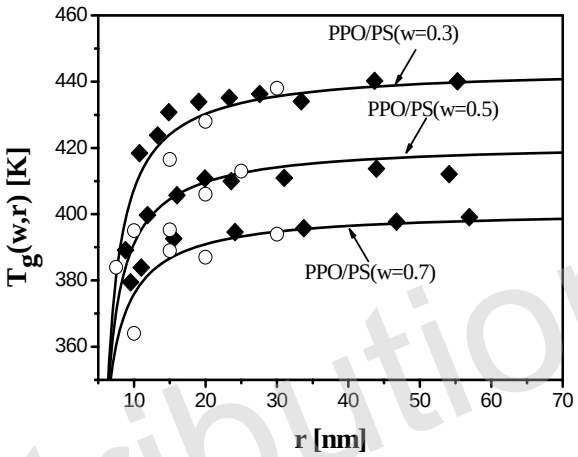

Fig. (8). $T_g(w,r)$ function of PPO/PS [poly(2,6-dimethyl-1,4-phenylene oxide)/polystyrene] blend films supported by a passivated Si (100) substrate in terms of Eqs. (35), (36) , and (39) with c_1 = 1/2 in Eq. (20) since the interaction between the film and the substrate interface is similar to that within polymers. For PPO, $T_g(0,\infty)$ = 483 K [94], $C_{pg}(\infty)$ = 1.591 J·g-atom^{-1}·K^{-1} [141], and $r_0 = \xi_1$ = 9 nm [141]. For PS, $T_g(1,\infty)$ = 375.15 K [139], $C_{pg}(\infty)$ = 1.919 J·g-atom^{-1}·K^{-1} [87], and $r_0 = \xi_1$ = 5 nm [91]. The symbols ♦ and O denote experimental and computer simulation results, respectively [142].

5.2.3. Néel, Ferromagnetic, Ferroelectric, and Superconductive Transition Temperature

Figs. (**9**) and (**10**) compare model predictions and experimental results for $T_N(r)$ function of NiO, CuO, Ho, and CoO with different surroundings. As shown in the figures, in the full size range, our model predictions are in good agreement with the experimental data.

Figs. (**11**), (**12**), and (**13**) compare the model predictions of Eq. (42) and the experimental results for $T_c(r)$ functions of ferromagnetic, ferroelectric, and superconductive nanocrystals where the related parameters are listed in Table **1**. Good agreements between Eq. (42) and experimental results for different substances, distinct transitions and different substrate conditions are found in a simple and unified form as long as the related thermodynamic parameters of crystals are known. Eq. (42) affords more facilities to predict $T_c(r)$ without any free parameter. Note that Co-Ni alloys can be roughly expressed as an algebraic sum of elements of which the alloys consist and $S_b \approx 13R$ has been proved to be a good approximation for compounds [99].

5.3. Melting Enthalpy

A comparison between Eq. (32) and experimental results for $H_m(r)$ function of In nanocrystals is shown in Fig. (**14**). A pretty agreement between them is got. $H_m(r)$ function has a similar form of $T_m(r)$ or $E_c(r)$. This result confirms the fact that $T_m(r) \propto H_m(r) \propto$

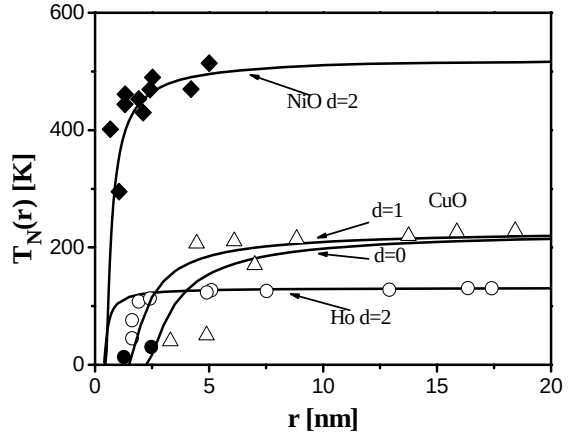

Fig. (9). $T_N(D)$ functions of NiO, CuO, and Ho in terms of Eq. (40). Necessary parameters are cited from the reference [143]. For NiO, $T_N(\infty)$ = 523 K, $\alpha_s = \alpha_i$ = 1.583 in terms of Eq. (23), r_0 = 0.421 nm, and the symbol ♦ denotes experimental results for NiO films [143]. For CuO, $T_N(\infty)$ = 229 K, $\alpha_s = \alpha_i$ = 1.563, r_0 = 1.369 nm and 2.054 nm for CuO nanorods with d = 1 and nanoparticles with d =2, respectively, and the symbols • and Δ denote experimental results for CuO nanorods and nanoparticles, respectively [143]. For Ho, $T_N(\infty)$ = 131.2 K, $\alpha_s = \alpha_i$ = 1.561, r_0 = 0.358 nm, and the symbol O denotes experimental data of Ho films [143].

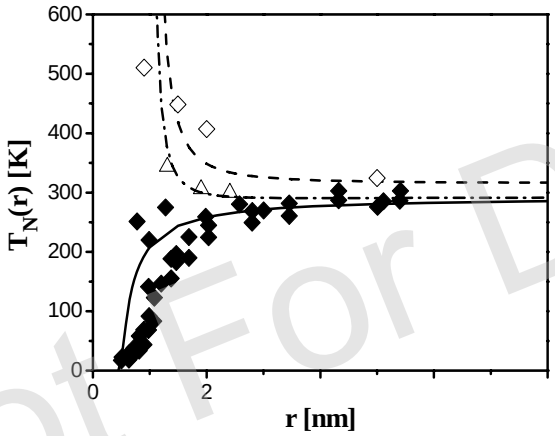

Fig. (10). $T_N(r)$ functions of CoO in terms of Eqs. (40), (23) and (41). Necessary parameters are cited from the reference [143]. The solid line denotes $T_N(r)$ of CoO films epitaxially grown on the SiO_2 substrate and the symbol ♦ denotes the corresponding experimental results [143]. $T_N(\infty)$ = 293 K, $\alpha_s = \alpha_i$ = 1.544, r_0 = 0.426 nm. The dashed and dash dotted lines denote $T_N(r)$ function of CoO films supported by NiO and Fe_3O_4 substrates, respectively, and the symbols ◊ and Δ denote the corresponding experimental results [143]. For CoO/NiO, α_i = 0.5544, and for CoO/Fe_3O_4, α_i = 0.4139.

$E_c(r)$ while $S_m(r)$ has a secondary effect on these energetic thermodynamic amounts.

5.4. Phase Diagram

5.4.1. Solution Phase Diagram for Binary System

Figs. (**15**), (**16**), (**17**), and (**18**) show continuous solution phase diagrams of different binary systems of metals Cu-Ni, semiconductors Ge-Si, ceramics Al_2O_3-Cr_2O_3 and organic crystals *p*-chlorobromobenzene-*p*-dibromobenzene in terms of Eqs. (48) and (49) where the parameters used are listed in Tables **2** and **3**. Except for Fig. (**16**) where $S_{vib}(\infty)$ is cited from the reference [80], $S_{vib}(\infty) \approx S_m(\infty) = H_m(\infty)/[nT_m(\infty)]$ is taken since the unit of $S_{vib}(\infty)$ is Jg-atom^{-1}K^{-1} [10]. n = 1 in Fig. (**15**), n = 5 in Fig. (**17**), and n = 12 in

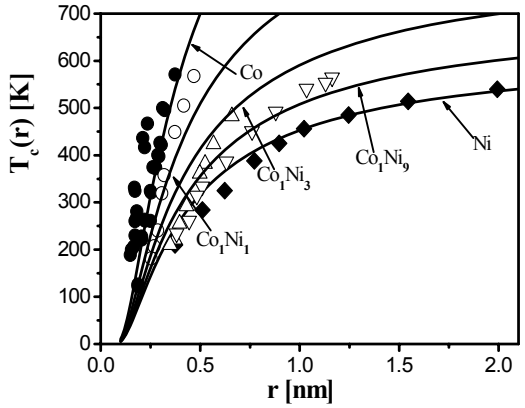

Fig. (11). $T_c(r)$ functions of Co, Ni, and Co-Ni alloys ferromagnetic ultrathin films on substrates with strong interactions between the thin films and the substrates. The solid lines denote the model predictions based on Eq. (42) where $r_0 = h/8$ with c_1 = 1/2 in terms of Eq. (34). The symbol ● [99] shows the experimental results of Co/Cu(100), Co/Cu(001) and Co/Cu(100) and the symbol ◆ [99] shows that of Ni/Cu(100). The symbols O, Δ and ∇ denote the experimental results of Co-Ni alloys Co_1Ni_1/Cu(100), Co_1Ni_3/Cu(100) and Co_1Ni_9/Cu(100), respectively [99].

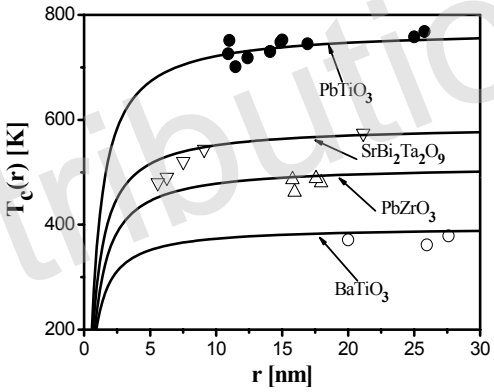

Fig. (12). $T_c(r)$ functions of $PbTiO_3$, $BaTiO_3$, $PbZrO_3$ and $SrBi_2Ta_2O_9$ ferroelectric nanocrystals. The solid lines denote the model predictions in terms of Eq. (42) where $r_0 = h/4$ with c_1 = 1 in terms of Eq.(34). The symbols ●, O, Δ, and ∇ show the experimental results of $PbTiO_3$, $BaTiO_3$, $PbZrO_3$, and $SrBi_2Ta_2O_9$, respectively [99].

Fig. (**18**). To determine $2r_0$, larger h values between two component counterparts are always taken in all figures as illustrated above. For molecules, $h = \sqrt[3]{V_c}$ where V_c is the volume of the cell [10]. For

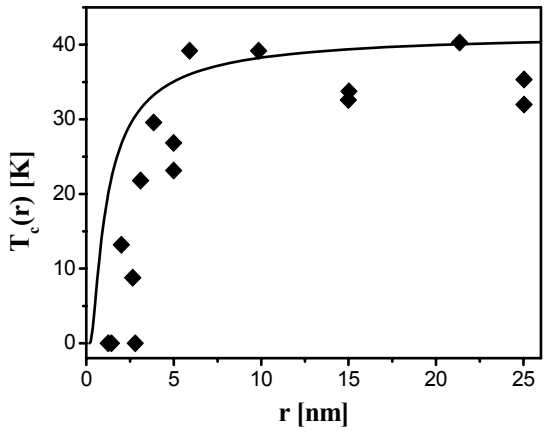

Fig. (13). $T_c(r)$ functions of MgB_2 superconductive nanocrystals. The solid lines denote the model predictions based on Eq. (42) where $r_0 = h/4$ with c_1 = 1 in terms of Eq. (34). The symbol ◆ [99] shows the experimental results of MgB_2.

Table 1. Necessary Parameters Used in Eq. (42) for Determining $T_c(\infty)$ Functions of Several Transitions. $T_c(\infty)$ is in K, E_b in KJ·g-atom^{-1}, T_b in K, S_b in J·g-atom^{-1}·K^{-1} and h is in nm

	$T_c(\infty)$	E_b [144]	T_b [144]	S_b[a]	h[b]
Co	1404 [145]	376.5	3201	117.62	0.2497
Ni	631 [145]	370.4	3187	116.22	0.2492
Co_1Ni_1[c]	1017.5			116.92	0.2495
Co_1Ni_3[c]	824.3			116.57	0.2493
Co_1Ni_9[c]	708.3			116.36	0.2493
$PbTiO_3$	773 [146]			13*R*	0.2830
$BaTiO_3$	396 [147]			13*R*	0.2430
$PbZrO_3$	513 [17][1]			13*R*	0.2880
$SrBi_2Ta_2O_9$	589 [148]			13*R*	0.2700
MgB_2	41.7 [149]			13*R*	0.3520

[a]For elements, $S_b = E_b/T_b$, while for compounds $S_b \approx 13R$ as a first order approximation which is equal to that of the mean value of the most elements (70-150 J·g-atom^{-1}·K^{-1}) [144].
[b]See the references for elements [8] and compounds [17].
[c]For Co-Ni alloys, the values of $T_c(\infty)$, S_b and h are calculated to a first order approximation as algebraic sum of the corresponding values for elements forming the alloys.

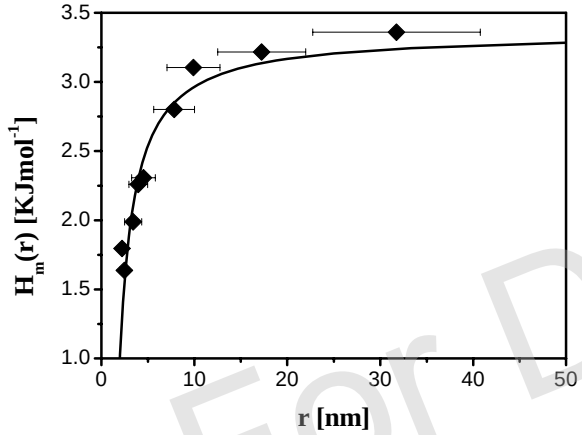

Fig. (14). $H_m(r)$ functions of disk-like In nanoparticles in terms of Eqs. (32) and (20) shown as the solid line and the symbol ♦ denotes the corresponding experimental results [150] where $H_m(\infty)$ = 3.36 KJ·mol^{-1} [151], d = 1 and other parameters see the caption of Fig. (**4**).

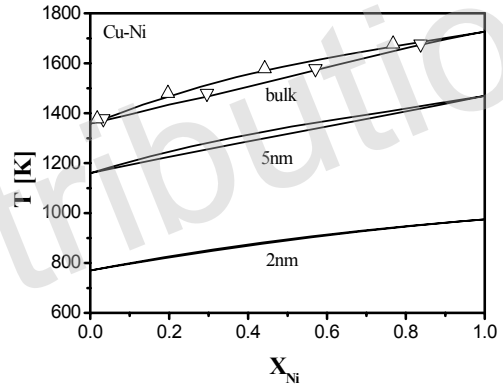

Fig. (15). Cu-Ni nano and bulk phase diagrams where the solid lines show the theoretical calculations for regular solution in terms of Eqs. (48) and (49) and the symbols Δ and ∇ denote the bulk experimental results [153]. To determine $\Omega^S(\infty)$ and $\Omega^L(\infty)$, T = 1573.15 K, $x_{1Ni}{}^L$ = 0.45 and $x_{1Ni}{}^S$ = 0.57 are used in the calculation.

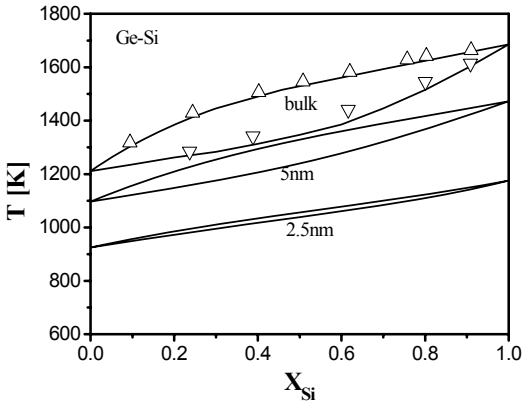

Fig. (16). Ge-Si nano and bulk phase diagrams where the solid lines show the theoretical calculation for regular solution in terms of Eqs. (48) and (49) and the symbols Δ and ∇ denote the bulk experimental results [154]. To determine $\Omega^S(\infty)$ and $\Omega^L(\infty)$, T = 1506.5 K, $x_{1Si}{}^L$ = 0.40 and $x_{1Si}{}^S$ = 0.73 are used in the calculation.

organic molecules, there is no direct value of V_c in literatures. V_c is thus determined by $V_c = M/(\rho N_a)$.

As shown in Figs. (**15**), (**16**), (**17**), and (**18**), although the chemical bonds between components in the above phase diagrams are different in nature, our model can be utilized in a unified form. This correspondence for any kind of continuous solution phase diagram is because the assumption that composition-independent Ω takes the small role where the electronegativity difference between two components is little. As r decreases, solidus and liquidus curves drop as $T_m(r)$ functions of each component decrease. Another evident change compared with the bulk phase diagram is the narrowing of the two-phase zone. As $r \rightarrow 2r_0$, which is about several nanometers, the zone even approaches zero since $\Omega(2r_0) \rightarrow 0$ where the regular solution deteriorates into the ideal solution and the structures of the liquid and the solid become similar because they have the same short-range order at this limit size.

The success of the model shown in Figs. (**15**), (**16**), (**17**), and (**18**) could be extended to deal with other related phase diagrams. Since the second-phase strengthening is one of the strengthening methods for structural materials, especially for nonferrous alloys, where the precipitated phase has the nanometer size while the solution phase remains in bulk. This is the problem to determine the solvus line in bulk phase diagrams with nanoprecipitation phase. This size difference leads to a larger solid solubility limit, which is

[1] Reference [17] is cited in both Table **1** and the text.

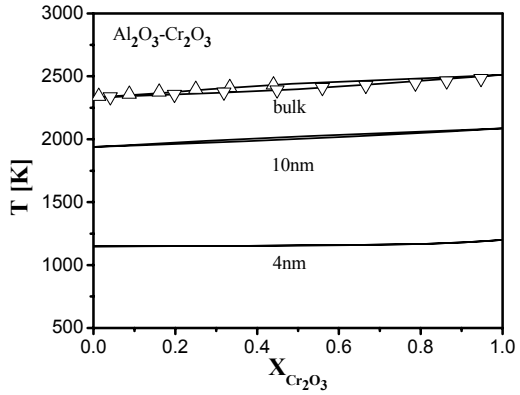

Fig. (17). Al_2O_3-Cr_2O_3 nano and bulk phase diagrams where the solid lines show the theoretical calculation for regular solution in terms of Eqs. (48) and (49) and the symbols Δ and ∇ denote the bulk experimental results [155]. To determine $\Omega^S(\infty)$ and $\Omega^L(\infty)$, T = 2430 K, $x_{1Cr2O3}{}^L$ = 0.44 and $x_{1Cr2O3}{}^S$ = 0.67 are used in the calculation.

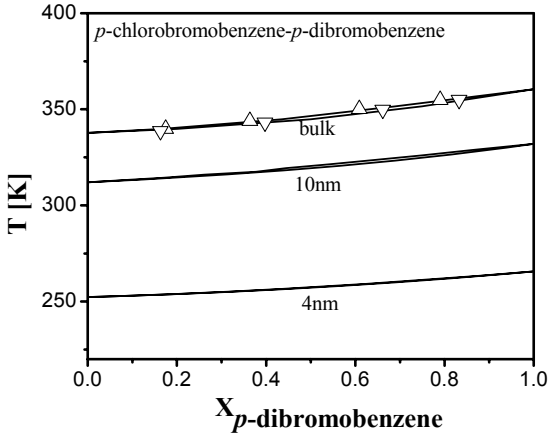

Fig. (18). *p*-chlorobromobenzene–*p*-dibromobenzene nano and bulk phase diagrams where the solid lines show the theoretical calculation for regular solution in terms of Eqs. (48) and (49) and the symbols Δ and ∇ denote the bulk experimental results [156]. To determine $\Omega^S(\infty)$ and $\Omega^L(\infty)$, T = 347.39 K, $x_{1p\text{-dbb}}{}^L$ = 0.50 and $x_{1p\text{-dbb}}{}^S$ = 0.57 are used in the calculation.

often found in industrial cases. According to the above deduction, we could consider the phase equilibrium between a bulk phase and a nanophase.

5.4.2. Bi-Layer Transition Diagram of Metallic Thin Multilayers

According to Eqs. (52) and (57), the predicted bi-layer diagrams for Co/Cr, and Zr/Nb multilayers are shown in Figs. (**19**) and (**20**) where experimental results and the bi-phase boundaries in light of experimental results are also shown. The parameters used in equations are listed in Tables **4** and **5**. Our predictions correspond to the experimental results well and are much better than the fitting results, which are plotted in the figures as dash lines. As shown in Figs. (**19**) and (**20**), when one layer has a thicker thickness than another, the structure of the other prefers to take the same structure of this layer. This is because when the same structure is adopted, the interface energy changes from γ_{in} to γ_c while the corresponding elastic energetic increase is smaller than the drop of interface energy.

5.4.3. Thermodynamic Phase Stabilities of Nanocarbon

In terms of Eq. (66) and other related equations, *r*-*T* phase diagram of nanocarbon are calculated and plotted in Fig. (**21**) where the related parameters are listed in Table **6**. As shown in Fig. (**21**), the predicted phase diagram is correspondent to experimental and other theoretical results. The disappearance of dangling bonds in ***F*** and ***O*** leads to significant drop of G^F and G^O, which stabilizes ***F*** and ***O*** when r is very small. The energetic increase caused by the dangling bonds in ***D*** is larger than the energetic drop induced by P_{in} at very small size. Because the contributions of γ_{sv} and f in different structures at different sizes on nanocarbons are distinct, nanocarbons undergo transitions in a series of **G→D→O(F)** or bonding of $sp^2 \rightarrow sp^3 \rightarrow sp^2$ with reducing size. This result confirms that diamond could stably exist when T and P are low and r is small and the low

Table 2. Related parameters and Data Used in Figs. (15) and (16). *r* nad *h* are in nm, T_m in K, H_m, Ω^S and Ω^L in J·mol^{-1} and S_{vib} in J·g-atom^{-1}·K^{-1}.

r		Cu	Ni	Ge	Si
∞	T_m [152]	1357.6	1726	1210.4	1685
	H_m [152]	13050	17470	36940	50550
	Ω^S	11376.21		7666.74	
	Ω^L	12219.46		7715.47	
	h [8][2]	0.2826	0.2754	0.351	0.3368
	S_{vib}	9.613	10.122	4.62 [80][2]	6.72 [80][2]
5	T_m	1160	1470	1096.7	1472.2
	H_m	8874.43	11930	24542.94	33135.53
	Ω^S	7518.31		4437.51	
	Ω^L	8075.6		4465.71	
2.5	T_m			1096.7	1472.2
	H_m			24542.94	33135.53
	Ω^S			1208.28	
	Ω^L			1215.96	
2	T_m	770.2	974.31		
	H_m	1959.7	2916.9		
	Ω^S	1731.46			
	Ω^L	1859.8			

[2] References [8], [80] are cited in both Table **2** and the text.

Table 3. Related Parameters and Data Used in Figs. (17), and (18) Where *p*-chlorobromobenzene and *p*-dibromobenzene are Respectively Abbreviated as *p*-cbb and *p*-dbb. *r* and *h* are in nm, T_m is in K, H_m, Ω^S and Ω^L in J·mol^{-1} and S_{vib} in J·g-atom^{-1}·K^{-1}.

r		Al_2O_3	Cr_2O_3	p-cbb	p-dbb
∞	T_m	2327 [155]	2512 [155]	337.73 [156]	360.45 [156]
	H_m	113040 [155]	117230 [155]	18760 [157]	20284 [158]
	Ω^S	22371.72		-3641.2	
	Ω^L	22733.72		-4214.99	
	h[a]	0.634	0.6618	0.5866	0.5971
	S_{vib}	9.716	9.344	4.63	4.69
10	T_m	1937.66	2086.4	312	332.16
	H_m	72032.54	73269.45	13627.4	14628.3
	Ω^S	13488.36		-2336.7	
	Ω^L	13706.61		-2704.93	
4	T_m	1148.04	1200.68	252.3	266.17
	H_m	5253.64	882.46	2996.64	2899.03
	Ω^S	163.31		-379.96	
	Ω^L	165.96		-439.83	

[a]To determine *h* value, the related data are V_{cAl2O3} = 0.2548 nm^3 and V_{cCr2O3} = 0.2898 nm^3 [159], $M_{p\text{-cbb}}$ = 191.46 g and $\rho_{p\text{-cbb}}$ = 1.576 g·cm^{-3} [160], $M_{p\text{-dbb}}$ = 235.92 g and $\rho_{p\text{-dbb}}$ = 1.841 g·cm^{-3} [160].

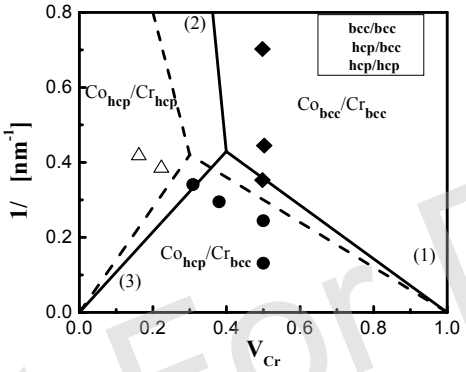

Fig. (19). The bi-phase diagram of Co/Cr multilayers where the solid lines denote model predictions in terms of Eqs. (52) and (57) and the dashed lines [108] are obtained by the experimental results shown as ♦, • and Δ. [169,170].

temperature synthesis of nanodiamond is a correct way without angst for the **D** → **G** transition.

agreement with the experimental results. Since the considered size is only several nanometers, this decrease is induced not only by the contribution of surface, but also by the increase of internal energy of atoms within the nanocrystals. Thus, the activity needed for diffusion is much smaller than the corresponding bulk.

Fig. (**23**) shows a comparison between Eq. (73) and experimental results for $D(r,T)$ function of N atoms diffusing into nanostructured bcc Fe. Although only one experimental point shown in the figure is difficult to supply the consistency of $D(r,T)$ function in the whole range of *r* with the experiment, this experimental point fits the model prediction. This dramatic enhancement of diffusion ability due to the drop of grain size leads to the possibility of surface chemical treatment of steels at 573 K, which is much lower than the usual treatment temperature of about 930 K.

6. CONCLUDING REMARKS

6.1. Attainment

Modeling for recent progress on $T_m(r)$ function is comparatively reviewed. Without any free parameter, our model based on Lindemann′s criterion, or enhancement or suppression of thermal

Table 4. The Related Parameters in Eqs. (52) and (57). *h* is in nm, T_m in K, H_m in kJ·mol^{-1}, V_m in cm^3·mol^{-1}, S_{vib} in J·mol^{-1}·K^{-1}, and $\Delta\mu$ is in J·m^{-3}.

	h [8][1]	T_m [161]	H_m [161]	V_m [161]	$\Delta V_m/V_s$	$S_{vib}(\infty)$	$\Delta\mu$
Cr	0.2498	2130	16.9	7.23	0.067	7.45	10.3×10^8 [162]
Co	0.2497	1768	16.19	6.7	0.035 [163]	7.93	6.3×10^8 [162]
Zr	0.3179	2125	16.9	14.1	0.035	8.64	3.7×10^8 [163]
Nb	0.2858	2740	26.4	10.87	0.055	8.05	9.2×10^8 [163]

Note: All *h* values are those of stable phases. When a metastable phase is present and when the corresponding *CN* is changed, *h* values change according to the Goldschmidt premise. $S_{vib}(\infty)$ are determined by Eq. (26) where $S_m(\infty)$ values are cited from the reference [112]. The unknown $\Delta V_m/V_s$ value of Zr is estimated to be 3.5% between that of Y and Nb according to its location in the Periodic Table of elements [164,165]. The values of $\Delta V_m/V_s$ of Cr and Nb are determined by $(1/\rho_l\text{-}1/\rho_s)\rho_s$-0.07 [166,167], where ρ_l and ρ_s are cited from references [8,168].

5.5. Diffusion Activation Energy and Diffusion Coefficient

Fig. (**22**) shows the model predictions of Eq. (72) and related experimental results of Ag into Au and Ag into Cu. As shown in Fig. (**22**), as *r* decreases, or χ increases, $E(r)$ drops. In light of the figure, the model predictions for $E(r)$ of different systems are in

vibrations of atoms of nanocrystals, has described both undercooling and superheating phenomena of nanocrystals. This model covers all essential considerations of early models with wider size

[1] Reference [8] is cited in both Table **4** and the text.

Table 5. The Calculated γ (J·m^{-2}) and m_i Values of the Considered Multilayer Systems. [During the Calculation of Eq. (52), $\Delta\gamma_1$ and $\Delta\gamma_3$ is taken as the Differences Between γ_{in} and γ_c, Which are Determined by Eq. (57); $\Delta\gamma_2 = \Delta\gamma_1 - \Delta\gamma_3$.]

	Co/Cr	Zr/Nb
γ_{in}	0.8109	0.7724
$\gamma_{bcc/bcc}$	0.3700	0.2620
$\gamma_{hcp/hcp}$	0.3320	0.2880
m_1	-0.715	-0.362
m_2	10	21.15
m_3	1.075	0.949

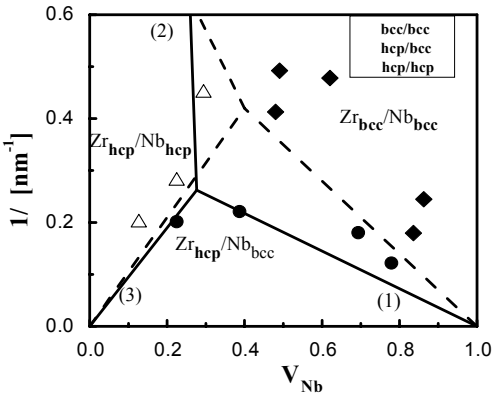

Fig. (20). The bi-phase diagram of Zr/Nb multilayers where the solid lines denote model predictions in terms of Eqs. (52) and (57) and the dashed lines are obtained by the experimental results shown as ♦, • and Δ [171,172].

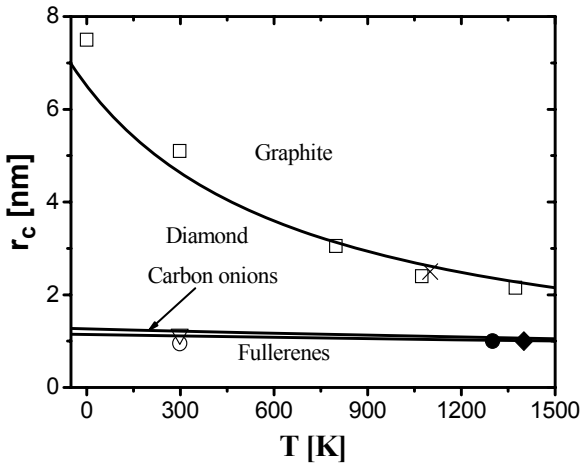

Fig. (21). The *r*-*T* transition diagram of nanocarbon in terms of Eq. (66) under $P = 0$ shown as the solid lines where other theoretical (O, ∇ [118], and □ [183]) and experimental results (● [123], ♦ [129], and [184]) are presented for comparison. $P(T) = (2.73T+2.02\times10^3)$ MPa [114,115].

grams including continuous binary solution phase diagrams, bi-phase transition diagrams of metallic thin multilayers, and solid transition phase diagrams have been constructed. As *r* decreases, phase diagrams exhibit evident difference from the corresponding bulk and are theoretically and experimentally meaningful due to its utility of prediction on phase structures of nanocrystals. Moreover, the model has been applied to predict $E(r)$ and $D(r)$ functions, which indicates an evident tendency of much more rapid kinetic process in comparison with the bulk case.

In all of the above extensions, reasonable agreements between model predictions and experimental data from systems with various bond natures have been reached, evidencing the validity of the

Table 6. The Thermodynamic Parameters of the Nanocarbon. *h* is in nm, V_m in cm^3·mol^{-1}, H_m, E_c, and E_V in kJ·mol^{-1}, T_m in K, S_m and S_{vib} in J·mol^{-1}·K^1, κ in 10^{-10}Pa^{-1} and *f* and γ are in J·m^{-2}

	D	G	F	O
h	0.154 [173]	0.142 [174]	0.157 [175]	
V_m	3.417 [173]	5.398 [173]	5.4r [175]	7.310 [176]
H_m	125 [177]	120 [128][1]	53 [178]	
T_m	3723 [126][1]	4800 [128][1]	1600 [178]	
S_m	33.58	25.00	33.12	
S_{vib}	6.37	4.75	6.29	
κ	0.088 [126][1]	1.000 [126][1]	0.212 [179]	
E_c		-714 [180]	-675 [180]	
f	6.10	1.10	$2.98/d^{1/2}$	
γ	3.70 [181,182]	3.27 [175]	0	0
E_V				5.4 [120][1]

Note: $S_m = H_m/T_m$. $S_{vib} \approx 0.19S_m$ is estimated as a mean proportion of Si and Ge since they belong to the same IVA group in the elemental table.

range suitability and may be extended to predict $H_m(r)$ and $E_c(r)$ functions. Moreover, $T_g(r)$ for glass transition and even binary polymer alloys, and $T_c(r)$ functions for ferromagnetic-antiferromagnetic, ferromagnetic, ferroelectric, and superconductor phase transitions are established. The obtained unified form of the functions reveals the physical nature of size dependence of materials properties and internal relationship among different types of phase transitions. Based on the above models, size-dependent phase diamodel. Further extension of this general model to other fields would be more beneficial.

It is found that the size dependence of properties of a system is indeed an independent thermodynamic amount. This result brings out an evident extension of the classic thermodynamics where the

[1]References [120], [126], [128] are cited in both Table **6** and the text.

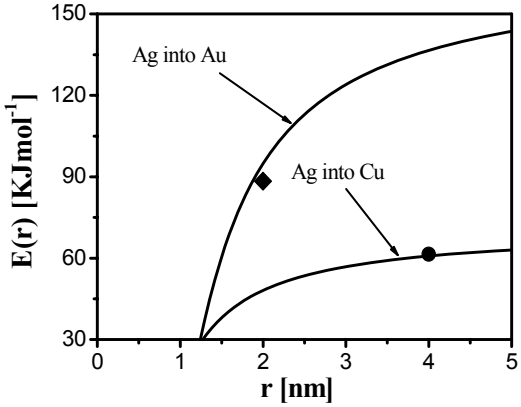

Fig. (22). $E(r)$ functions of Ag diffusing into Au and Ag diffusing into Cu in terms of Eq. (72) shown as the solid lines. The parameters used are cited from the reference [185]. For Ag into Au, $E(\infty)$ = 168.84 KJ·mol^{-1}, $S_{vib}(\infty)$ = 9.157 J·mol^{-1}·K^{-1}, and h = 0.2884 nm. The symbol ♦ denotes the corresponding experimental result [73]. For Ag into Cu, $E(\infty)$ = 101.76 KJ·mol^{-1}, $S_{vib}(\infty)$ = 9.157 J·mol^{-1}·K^{-1}, and h = 0.2238 nm. The symbol • denotes the corresponding experimental result [186].

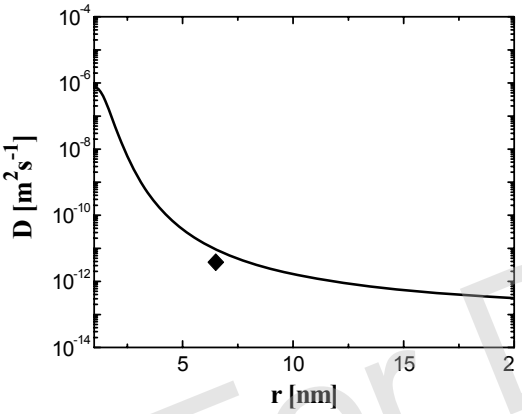

Fig. (23). $D(r,T)$ function of N diffusing into bcc nanostructured Fe in terms of Eq. (73) shown as the solid line where T = 573 K. The parameters used are cited from the reference [187]. $D_0 = 7.46\times10^{-7}$ m^2·s^{-1}, $E(\infty)$ = 78.3 KJ·g-atom^{-1}, $S_{vib}(\infty)$ = 36.106 J·g-atom^{-1}·K^{-1}, and h = 0.2483 nm. The symbol ♦ denotes the corresponding experimental result [71].

studied system of the thermodynamics can cover all size range from microscopic, along mesoscopic, to macroscopic size, as long as the solid remains the bulk stable structure or other metastable structure. This is not only the most progress of the thermodynamics, but also especially beneficial for the research on nanoscience and nanotechnology nowadays. This progress clarifies also the always importance of the classic thermodynamics, which could keep up with the time.

6.2. Limitation

It is well known that thermodynanics has a statistic mechanics basis. Thus, as a system drops to several nanometers or a system consists of only several ten to several hundred molecules, the statistic meaning disappears. In addition, as size of a system decreases, a crystalline structure is no more stable due to its big bond deficit where a cluster with special structure arises. Under this condition, bond order and bond strength vary, which lead to all thermodynamic size-dependent functions to be disabled since the models assume that the structure of the concerned solids remains as the size decreases. Up to now, only computer simulation could be used to exactly determine the above mentioned structures and thus the corresponding functions, which have not any direct relation with the corresponding bulk ones and cannot be described by an analytical solution.

The most low-dimensional materials are attached on substrates. Thus, interface effect due to the existence of film/substrate interface takes the role on the thermodynamic properties of nanocrystals. Since the interface combination, chemically and mechanically, depends on not only the composition and the structure of the low dimensional materials, but also experimental and technic conditions, the predicted results cannot fully correspond to experimental results while the model prediction considers only the thermodynamic properties under an ideal condition. Even the interface is ideally combined, the chemical interface bonding is only assumed to be strong and weak in our model, which is a too rough estimation. This is also the case for the estimation of interface stress where nonlinear mechanical action widely exists.

It is known that alloys are widely used in industry since the alloying could better satisfy the property requirement for parts and devices in industry especially when the mechanical properties are mainly considered. This consideration even exists in semiconductor industry, such as liners in IC. However, Ω function is difficult to determine due to its complicity for bond interaction when the value of Ω(∞) is big. This is the reason why in the above sections only the elements, the compounds, and the alloys with weak chemical interactions are concerned. Luckily, the interaction among different molecules become weaker as r decreases. This characteristic brings out lower error when the above models are utilized for nanosystems even the systems consist of two or more components.

In our models, the energetic contribution of surface (interface) molecules is considered as the most essential size effect. However, for thin films, especially when the thickness of the thin films is larger than 10-20 nm, the additional contribution of grain boundary within the thin films on the size effect is present, which is extra true for electronic or electric properties of thin films. Although as a rough estimation, the contribution of grain boundary is about one third of the surface since the incoherent interface energy is about one third of the surface energy, grain size is not a certain thermodynamic function of the film thickness, which strongly depends on the kinetic condition during the formation or fabrication of the thin films. Thus, surface/interface ratio is not a thermodynamic amount. Note that when the electric conductivity of thin films is considered, the interface effect on the electric conductivity could be stronger than the above mentioned fraction of surface, which becomes evident as r increases.

Since the surface stress induces the internal pressure for low dimensional materials, surface stress is always an important effect on properties of nanomaterials. Note that the internal pressure is a natural phenomenon related with the bond contraction of surface atoms, and does not certainly depend on the curvature of the nanomaterials. Thus, there exists internal pressure even on a flat film. In addition, our quantitative modeling on surface stress has indeed been extended to determine T-P phase diagram since the internal pressure has the same effect of the external pressure [188,189]. However, although we have modeled this amount, the given equation is only a rough estimation and need further work on it. In particular, when there exist electronic charges on the surface, our model for surface stress leads to big errors.

6.3. Prospect

As nanothermodynamics on phase transitions develops, a more complete understanding of the thermodynamic and the kinetic aspects for nanomaterials could be carried out. These works will help us to understand the thermal stability of nanomaterials that is a very important property for their application of nanomaterials due to their metastable nature. In addition, since the mechanic, optic, magnetic and electronic properties of nanomaterials are functions of their structures, the phase transition temperatures decide the limit application temperature range and also the necessary size of nano-

materials. Thus, the above theory is important for the application of nanomaterials. However, the above mentioned limits restrict the full comprehending and exact quantitative prediction. Thus, the above limits should be solved one by one.

The above theory has established a good way for the top-down calculation, which can analytically obtain thermodynamic mesoscopic and even microscopic properties. The thermodynamics with the size effect covers almost full size range from nanometer to centimeter while its physical basis is at a molecular level. Note that since we are familiar with the bulk thermodynamics and related properties, its extending to nanometer size in this means can be better understood and better utilized in a natural art.

The theory is also a good complementarity for the widely used bottom-up method of computer simulation. The computer simulation is based on potential of atoms, which gives more electronic message of atoms and helps us to understand the physical nature of matters at the electronic level. However, the coverage of materials size using computer simulation technique is small due to the limitation of the computer calculation ability. Moreover, the reliability of the computer simulation at present depends on strongly the given potential, which achieves progress only gradually although this progress is fast than the computer calculation ability. As computer calculation ability increases, which is decided by Moore rule, the importance of the nanothermodynamics gently decreases. However, the nanothermodynamics still takes its special role in the known future.

A special emphasis here is given for the melting phenomenon. Although the melting is a well known natural phenomenon, its physical nature is still in question. The Lindemann′s criterion, which is the basis of the above theory, has given a thermodynamic melting temperature although the criterion in nature is a kinetic melting one. A simple interpretation of the criterion could be considered as that the melting temperature is a kinetic melting temperature of the surface, which leads to a thermodynamic melting within the crystals. Further work should reveal the nature of the melting and why Lindemann′s criterion is correct.

Fabrication of patterns directly on substrates shows a wonderful and an essential way for IC and MEMS manufacture and denotes the future of nanotechnology. This technique combines the both manufacture procedures of row materials production and device fabrication, and exhibits thus the spirit of the environment-friendly manufacture. Since the quantum effect at this case becomes evident [190] and statistic basis of the thermodynamics results in larger error due to the small size of patterns, the application of nanothermodynamics in this field will be a chanllenge and need to come to more attention.

ACKNOWLEDGEMENTS

The financial supports by National Key Basic Research and Development Program (Grant No. 2004CB619301) and by ″985 Project″ of Jilin University are acknowledged.

NOMENCLATURE

a	=	Activity
A	=	Surface or interface area
A_0	=	Surface atom density
A_m	=	Molar surface area
b	=	Burgers vector
B	=	bucky diamond
c	=	Constant. For special cases, Arabic number as subscript is used.
c_i	=	*CN*-dependent reduction of bond length
C_{pg}	=	Heat capacity difference between liquid and glass at T_g
CN	=	Coordination number
C_p	=	Specific heat capacity of crystals
C_{pm}	=	Heat capacity difference between liquid and crystal at T_m
d	=	Dimension of crystals
$D(r,T)$	=	Self-diffusion or intrinsic diffusion coefficient of interdiffusion
$D_0(r)$	=	A pre-exponential constant
D	=	Diamond
$E(r)$	=	Activation enthalpy
E_b	=	Bulk evaporation enthalpy
E_c	=	Cohesive energy
E_v	=	Molar van der Waals interlayer attraction
$E_{exc}(T)$	=	Spin-spin exchange interaction
$E_v(T)$	=	Thermal vibration energy
f	=	Activity coefficient
f_s	=	Surface stress
f_B	=	Volume fraction of element B in the multilayer
$F(r)$	=	A size dependent function during the deduction of $T_m(r)$ function
F	=	Fullerenes
g	=	Shear modulus
G	=	Gibbs free energy
G_e	=	Molar elastic free energy
G_l	=	Gibbs free energy of liquid
G_m	=	Melting Gibbs free energy
G_s	=	Gibbs free energy of crystals
G_v	=	Molar volume Gibbs free energy
G	=	Graphite
h	=	Atomic or molecular diameter (the nearest atomic or molecular spacing)
H_m	=	Melting enthalpy
k	=	Boltzmann′s constant
l	=	Length of the dislocation
M	=	Atomic or molecular molar weight
m	=	A parameter varying with the bond nature
m_1, m_2, m_3	=	Slopes of lines for binary multilayer diagrams
m_a	=	Atomic mass
n	=	Atom number
N	=	Number of molecules
N_a	=	Avogadro constant
N_d	=	Dislocation number
N^F	=	Carbon atom number of fullerenes
O	=	carbon onions
p	=	Planck′s constant
P	=	Pressure
P_{in}	=	Size-induced internal pressure

r	=	Radius of nanoparticles
r_0	=	A critical radius at which all atoms are located on the surface
R	=	Ideal gas constant
S	=	Entropy
S_a	=	Activation entropy
S_b	=	Bulk evaporation entropy
S_{conf}	=	Configurational melting entropy
S_{el}	=	Electronic melting entropy
S_m	=	Melting entropy
S_{vib}	=	Vibrational melting entropy
T	=	Absolute temperature
T_b	=	Bulk evaporation temperature
T_c	=	Critical temperatures of ferromagnetic, ferroelectric, and superconductor transition
T_g	=	Glass transition temperature
T_m	=	Melting temperature
U	=	Internal energy
u_d	=	Misfit dislocation energy of a single dislocation
V	=	Volume denoted by different subscripts
V_a	=	$(V_s+V_l)/2$
w	=	Weight fraction of the second component
x	=	Atomic percentage of a component in a binary system
y	=	Volume percentage of atoms in liquid
z_b	=	The bulk coordinate
z_i	=	The surface coordinate
z_{ib}	=	$z_{ib} = z_i/z_b$
∞	=	Bulk size
α	=	$\alpha = \sigma_{sa}^2/\sigma_{va}^2$ with $\sigma_{sa}^2/\sigma_{va}^2$ denoting the mean-square displacement of surface atoms and interior atoms
β_{ij}	=	Volume or number ratio of the *i*th atomic layer to that of the entire crystal
γ	=	Surface or interface energy denoted by different subscripts
δ	=	Layer thickness of surface melting
Δ	=	Difference between two physical amounts
η	=	A half of the distance of two adjacent dislocations
ε	=	Bond energy
θ	=	Contact angle between a particle and the matrix
Θ_E	=	Einstein temperature
Θ_D	=	Debye temperature
λ	=	Bi-layer thickness
μ	=	Chemical potentials
ν_f	=	Vibrational frequency
ν	=	Poisson ratio
ν_E	=	Einstein frequency
ξ	=	Correlation length of solid-liquid interface
ξ_1	=	Correlation length for intermolecular cooperative rearrangement
ρ	=	Mass density
σ	=	Root-mean-square (rms) average amplitude of atomic thermal vibration
σ_c	=	Electronic conductivity
χ	=	Surface/volume ratio
φ	=	activity coefficient
ω	=	$\omega=\Omega/z$
Ω	=	Atomic interaction energy

REFERENCES

[1] Gibbs, J.W. *Trans. Conn. Acad.*, **1878**, *3*, 343.
[2] Rusanov, A.I. *Surf. Sci. R.*, **1996**, *23*, 173.
[3] Wang, C.X.; Yang, G.W. *Mater. Sci. Eng. R.*, **2005**, *49*, 157.
[4] Hill, T.L. *Nano Lett.*, **2001**, *1*, 273.
[5] Dash, J.G. *Rev. Mod. Phys.*, **1999**, *71*, 1737.
[6] Lindemann, F.A. *Z. Phys.*, **1910**, *11*, 609.
[7] Stillinger, F.H. *Science*, **1995**, *267*, 1935.
[8] King, H.W. Physical Metallurgy, 3rd ed., Cahn, R.W. and Haasen, P. Ed.; North-Holland Physics Publishing: Amsterdam, **1983**, pp. 63.
[9] Sun, C.Q.; Wang, Y.; Tay, B.K.; Li, S.; Huang, H.; Zhang, Y.B. *J. Phys. Chem. B*, **2002**, *106*, 10701.
[10] Jiang, Q.; Shi, H.X.; Zhao, M. *J. Chem. Phys.*, **1999**, *111*, 2176.
[11] Cahn, R.W. *Nature*, **1986**, *323*, 668.
[12] Born, M. *J. Chem. Phys.*, **1939**, *7*, 591.
[13] Jin, Z.H.; Gumbsch, P.; Lu, K.; Ma, E. *Phys. Rev. Lett.*, **2001**, *87*, 055703.
[14] Hoffmann, H.J. *Materialwiss. Werkst.*, **2003**, *34*, 571.
[15] Pauchard, L.; Bonn, D.; Meunier, J. *Nature*, **1996**, *384*, 145.
[16] Burakovsky, L.; Preston, D.L. *Solid State Commun.*, **2003**, *115*, 341.
[17] Sun, C.Q.; Zhong, W.H.; Li, S.; Tay, B.K. *J. Phys. Chem. B*, **2004**, *108*, 1080.
[18] Gleiter, H. *Acta Mater.*, **2000**, *48*, 1.
[19] Lu, K. *Mater. Sci. Eng. R.*, **1996**, *16*, 161.
[20] Hasegawa, M.; Watabe, M.; Hoshino, K. *J. Phys. F: Met. Phys.*, **1980**, *10*, 619.
[21] Shi, F.G. *J. Mater. Res.*, **1994**, *9*, 1307.
[22] Goldstein, A.N.; Echer, C.M.; Alivisatos, A.P. *Science*, **1992**, *256*, 1425.
[23] Goldstein, A.N. *Appl. Phys. A*, **1996**, *62*, 33.
[24] Jackson, C.L.; McKenna, G.B. *J. Chem. Phys.*, **1990**, *93*, 9002.
[25] Jackson, C.L.; McKenna, G.B., *Chem. Mater.*, **1996**, *8*, 2128.
[26] Takagi, M. *J. Phys. Soc. Japan*, **1954**, *9*, 359.
[27] Chattopadhyay, K.; Goswami, R. *Prog. Mater. Sci.*, **1997**, *42*, 287.
[28] Thoft, N.B.; Bohr, J.; Buras, B.; Johnson, E. Johansen, A. *J. Phys. D: Appl. Phys.*, **1995**, *28*, 539.
[29] Sheng, H.W.; Ren, G.; Peng, L.M.; Hu, Z.Q.; Lu, K. *Phil. Mag. Lett.*, **1996**, *73*, 179.
[30] Sheng, H.W.; Ren, G.; Peng, L.M.; Hu, Z.Q.; Lu, K. *J. Mater. Res.*, **1997**, *12*, 119.
[31] Ercolessi, F.; Andreoni, W.; Tosatti, E. *Phys. Rev. Lett.*, **1991**, *66*, 911.
[32] Lutsko, J.F.; Wolf, D.; Phillpot, S.R.; Yip, S. *Phys. Rev. B*, **1989**, *40*, 2841.
[33] Broughton, J. *Phys. Rev. B*, **1992**, *46*, 2523.
[34] Hill, T.L. *Nano Lett.*, **2001**, *1*, 159.
[35] Hill, T.L. *Thermodynamics of small systems*, vol. I, Benjamin, W.A. New York, NY, **1963**.
[36] Hill, T.L. Thermodynamics of small systems, vol. II, Benjamin, W.A. New York, NY, **1964**.
[37] Tsallis, C. *J. Stat. Phys.*, **1988**, *52*, 479.
[38] Rajagopal, A.K. *Phys. Lett. A*, **1996**, *214*, 127.
[39] Yang, C.C.; Li, J.C.; Jiang, Q. *Chem. Phys. Lett.*, **2003**, *372*, 156.
[40] Zhang, D.L.; Cantor, B. *Acta Metall. Mater.*, **1991**, *39*, 1595.
[41] Zhang, L.; Zhang, L.H.; Sui, M.L.; Tan, J.; Lu, K. *Acta Mater.*, **2006**, *54*, 3553.
[42] Saka, H.; Nishikawa, Y.; Imura, T. *Phil. Mag. A*, **1988**, *57*, 895.
[43] Gråbaek, L.; Bohr, J. *Phys. Rev. Lett.*, **1990**, *64*, 934.
[44] Zhang, L.; Jin, Z.H.; Zhang, L.H.; Sui, M.L.; Lu, K. *Phys. Rev. Lett.*, **2000**, *85*, 1484.
[45] Zhong, J.; Zhang, L.H.; Jin, Z.H.; Sui, M.L. Lu, K. *Acta Mater.*, **2001**, *49*, 2897.
[46] Reiss, H.; Wilson, I.B. *J. Colloid Sci.*, **1948**, *3*, 551.
[47] Pluis, B.; Frenkel, D.; van der Veen, J.F. *Surf. Sci.*, **1990**, *239*, 282.
[48] David, T.Ben.; Lereah, Y.; Deutscher, G.; Kofmans, R.; Cheyssac, P. *Phil. Mag. A*, **1995**, *71*, 1135.
[49] Pawlow, P. *Z. Phys. Chem.*, **1909**, *65*, 545.
[50] Peters, K.F.; Cohen, J.B.; Chung, Y.-W. *Phys. Rev. B*, **1998**, *57*, 13430.
[51] Jones, D.R.H. *J. Mater. Sci.*, **1974**, *9*, 1.
[52] Jiang, Q.; Shi, H.X.; Zhao, M. *Acta Mater.*, **1999**, *47*, 2109.

[53] Couchman, P.R.; Jesser, W.A. *Nature*, **1977**, *269*, 481.
[54] Frenken, J.W.M.; van der Veen, J.F. *Phys. Rev. Lett.*, **1985**, *54*, 134.
[55] Semenchenko, V.K. *Surface Phenomena in Metals and Alloys*, Pergamon: Oxford, **1961**, pp. 281.
[56] Wen, Z.; Zhao, M.; Jiang, Q. *J. Phys. Chem. B*, **2002**, *106*, 4266.
[57] Bréchignac, C.; Busch, H.; Cahuzac, Ph.; Leygnier, J., *J. Chem. Phys.*, **1994**, *101*, 6992.
[58] Näher, U.; BjØrnholm, S.; Frauendorf, S.; Garcias, F.; Guet, C. *Phys. Rep.*, **1997**, *285*, 245.
[59] Nanda, K.K.; Sahu, S.N.; Behera, S.N. *Phys. Rev. A*, **2002**, *66*, 013208.
[60] Sun, C.Q. *Prog. Mater. Sci.*, **2003**, *48*, 521.
[61] Sun, C.Q.; Li, C.M.; Bai, H.L.; Jiang, E.Y. *Nanotechnology*, **2005**, *16*, 1290.
[62] Sun, C.Q.; Shi, Y.; Li, C.M.; Li, S.; Au Yeung, T.C. *Phys. Rev. B*, **2006**, *73*, 075408.
[63] Wautelet, M. *J. Phys. D: Appl. Phys.*, **1991**, *24*, 343.
[64] Wautelet, M.; Dauchot, J.P.; Hecq, M. *J. Phys. Condens. Matter*, **2003**, *15*, 3651.
[65] Shirinyan, A.; Wautelet, M.; Belogorodsky, Y. *J Phys. Condens. Matter*, **2006**, *18*, 2537.
[66] Qi, W.H.; Wang, M.P. *Mater. Chem. Phys.*, **2004**, *88*, 280.
[67] Kim, H.K.; Huh, S.H.; Park, J.W.; Jeong, J.W.; Lee, G.H. *Chem. Phys. Lett.*, **2002**, *354*, 165.
[68] Vallée, R.; Wautelet, M.; Dauchot, J.P.; Hecq, M. *Nanotechnology*, **2001**, *12*, 68 and references therein.
[69] Tanaka, T.; Hara, S. *Z. Metallkd.*, **2001**, *92*, 11 and references therein.
[70] Ouyang, G.; Tan, X; Wang, C.X.; Yang, G.W. *Nanotechnology*, **2006**, *17*, 4257.
[71] Tong, W.P.; Tao, N.P.; Wang, Z.B.; Lu, J.; Lu, K. *Science*, **2003**, *299*, 686.
[72] Dick, K.; Dhanasekaran, T.; Zhang, Z.; Meisel, D. *J. Am. Chem. Soc.*, **2002**, *124*, 2312.
[73] Shibata, T.; Bunker, B.A.; Zhang, Z.; Meisel, D.; Vardeman II, C.F.; Gezelter, J.D. *J. Am. Chem. Soc.*, **2002**, *124*, 11989.
[74] Hoshino, K.; Shimamura, S. *Phil. Mag. A*, **1979**, *40*, 137.
[75] Zhang, Z.; Li, J.C.; Jiang, Q. *J. Phys. D: Appl. Phys.*, **2000**, *33*, 2653.
[76] Jiang, Q.; Lang, X.Y. *Marcromol. Rapid Comm.*, **2004**, *25*, 825 and references therein.
[77] Mott, N.F. *Proc. R. Soc. A*, **1934**, *146*, 465.
[78] Jiang, Q.; Zhang, Z.; Li, J.C. *Chem. Phys. Lett.*, **2000**, *322*, 549.
[79] Wen, Z.; Zhao, M.; Jiang, Q. *Mater. Lett.*, **2003**, *57*, 2515.
[80] Regel′, A.R.; Glazov, V.M. *Semiconductors*, **1995**, *29*, 405.
[81] Jiang, Q.; Zhou, X.H.; Zhao, M. *J. Chem. Phys.*, **2002**, *117*, 10269.
[82] Zhang, Z.; Zhao, M.; Jiang, Q. *Semicond. Sci. Tech.*, **2001**, *16*, L33.
[83] Battezzati, L.; Greer, A.L. *Acta Metall. Mater.*, **1989**, *37*, 1791.
[84] Zhao, M.; Jiang, Q. *Solid State Commun.*, **2004**, *130*, 37.
[85] Jiang, Q.; Li, J.C.; Chi, B.Q. *Chem. Phys. Lett.*, **2002**, *366*, 551.
[86] Sun, C.Q.; *Prog. Solid State Chem.*, **2007**, *35*, 1.
[87] Jiang, Q.; Shi, H.X.; Li, J.C. *Thin Solid Films.*, **1999**, *354*, 283.
[88] Malinovsky, V.K.; Novikov, V.N. *J. Phys.: Condens. Matter*, **1992**, *4*, L139.
[89] Novikov, V.N.; Rössler, E.; Malinovsky, V.K.; Surovtsev, N.V. *Europhys. Lett.*, **1996**, *35*, 289.
[90] Forrest, J.A.; Mattsson, J. *Phys. Rev. E*, **2000**, *61*, R53.
[91] Forrest, J.A.; Dalnoki-Veress, K. *Adv. Colloid Interface Sci.*, **2001**, *94*, 167.
[92] Forrest, J.A.; Dalnoki-Veress, K.; Stevens, J.R.; Dutcher, J.R. *Phys. Rev. Lett.*, **1996**, *77*, 2002.
[93] Forrest, J.A.; Dalnoki-Veress, K.; Dutcher, J.R.; *Phys. Rev. E*, **1997**, *56*, 5705.
[94] Kim, J.H.; Jang, J.; Lee, D.-Y.; Zin, W.-C. *Macromolecules*, **2002**, *35*, 311.
[95] Fox, T.G. *Bull. Am. Phys. Soc.*, **1956**, *1*, 123.
[96] Aguilera-Granja, F.; Morán-López, J.L. *Solid State Commun.*, **1990**, *74*, 155.
[97] Zhong, W.H.; Sun, C.Q.; Tay, B.K.; Li, S.; Bai, H.L.; Jiang, E.Y. *J. Phys.: Condens. Matter*, **2002**, *14*, L399.
[98] Zhong, W.H.; Sun, C.Q.; Li, S.; Bai, H.L.; Jiang, E.Y. *Acta Mater.*, **2005**, *53*, 3207
[99] Yang, C.C.; Jiang, Q. *Acta Mater.*, **2005**, *53*, 3305.
[100] Zhang, R.; Willis, R.F. *Phys. Rev. Lett.*, **2001**, *86*, 2665.
[101] Guisbiers, G.; Wautelet, M. *Nanotechnology*, **2006**, *17*, 2008.
[102] Abudukelimu, G.; Guisbiers, G.; Wautelet, M. *J. Mater. Res.*, **2006**, *21*, 2829.
[103] Gaskell, D.R. *Physical Metallurgy* 3rd ed., Cahn, R.W. and Haasen, P. Ed.; Amsterdam: North-Holland, **1983**, pp. 300.
[104] Sun, C.Q.; Tay, B.K.; Lau, S.P.; Sun, X.W.; Zeng, X.T.; Li, S.; Bai, H.L.; Liu, H.; Liu, Z.H.; Jiang, E.Y. *J. Appl. Phys.*, **2001**, *90*, 2615.
[105] Müller, H.; Opitz, Ch.; Strickert, K.; Skala, L. *Z. Phys. Chem. Leipz.*, **1987**, *268*, 625.
[106] Mbaye, A.A.; Wood, D.M.; Zunger, *Phys. Rev. B*, **1998**, *37*, 3008.
[107] Redfield, A.C.; Zangwill, A.M. *Phys. Rev. B*, **1986**, *34*, 1378.
[108] Dregia, S.A.; Banerjee, R.; Fraser, H.L. *Scripta Mater.*, **1998**, *39*, 217.
[109] Kotzé, I.A.; Kuhlmann-Wilsdorf, D. *Appl. Phys. Lett.*, **1966**, *9*, 96.
[110] Hirth, J.P.; Lothe, J. *Theory of dislocations*, Wiley: New York, **1982**, pp. 59-96.
[111] Goldschmidt, V.M. *Ber. Deut. Chem. Ges.*, **1927**, *60*, 1263.
[112] Thompson, G.B.; Banerjee, R.; Dregia, S.A.; Fraser, H.L. *Acta Mater.*, **2003**, *51*, 5285.
[113] Liang, L.H.; Liu, D.; Jiang, Q. *Nanotechnology*, **2003**, *14*, 438.
[114] Bundy, F.P.; Bassett, W.A.; Weathers, M.S.; Hemley, R.J.; Mao, H.K.; Goncharov, A.F. *Carbon*, **1996**, *34*, 141.
[115] Palnichenko, A.V.; Jonas, A.M.; Chaarlier, J.-C.; Aronin, A.S.; Issi, J.P. *Nature*, **1999**, *402*, 162.
[116] Zaiser, M.; Banhart, F. *Phys. Rev. Lett.*, **1997**, *79*, 3680.
[117] Banhart, F.; Ajayan, P.M. *Nature*, **1996**, *382*, 433.
[118] Barnard, A.S.; Russo, S.P.; Snook, I.K. *J. Chem. Phys.*, **2003**, *118*, 5094.
[119] Barnard, A.S.; Russo, S.P.; Snook, I.K. *Phil. Mag. Lett.*, **2003**, *83*, 39.
[120] Barnard, A.S.; Russo, S.P.; Snook, I.K. *Phys. Rev. B*, **2003**, *68*, 073406.
[121] Fugaciu, F.; Hermann, H.; Seifert, G. *Phys. Rev. B*, **1999**, *60*, 10711.
[122] Hermann, H.; Fugaciu, F.; Seifert, G. *Appl. Phys. Lett.*, **2001**, *79*, 63.
[123] Kuznetsov, V.L.; Ziberberg, I.L.; Butenko, Y.V.; Chuvilin, A.L. *J. Appl. Phys.*, **1999**, *86*, 863.
[124] Nuriel, S.; Liu, L.; Barber, A.H.; Wagner, H.D. *Chem. Phys. Lett.*, **2005**, *404*, 263.
[125] Jiang, Q.; Liang, L.H.; Zhao, D.S. *J. Phys. Chem. B*, **2001**, *105*, 6275.
[126] Zhao, D.S.; Zhao, M.; Jiang, Q. *Diam. Relat. Mater.*, **2002**, *11*, 234.
[127] Wang, C.X.; Yang, Y.H.; Xu, N.S.; Yang, G.W. *J. Am. Chem. Soc.*, **2004**, *126*, 11303.
[128] Savvatimskiy, A.I. *Carbon*, **2005**, *45*, 1115.
[129] Kuznetsov, V.L.; Chuvili, A.L.; Butenko, Y.V.; Stankus, S.V.; Khairulin, R.A.; Gutakovskii, A.K. *Chem. Phys. Lett.*, **1998**, *289*, 353.
[130] Liang, L.H.; Shen, C.M.; Chen, X P.; Liu, W.M.; Gao, H.J. *J. Phys.: Condens. Matter*, **2004**, *16*, 267.
[131] http://www.webelements.com/
[132] Ubbelohde, R. *Melting and Crystal Structure*, Clarendon press: Oxford, **1965**, pp. 171.
[133] Jiang, Q.; Zhang, S.; Zhao, M. *Mater. Chem. Phys.*, **2003**, *82*, 225 and references therein.
[134] Jiang, Q.; Zhang, Z.; Li, J.C. *Acta Mater.*, **2000**, *48*, 4791.
[135] Jiang, Q.; Liang, L.H.; Li, J.C. *J. Phys.: Condens. Matter*, **2001**, *13*, 565.
[136] Barin, I.; Knacke, O. *Thermochemical Properties of Inorganic Substances*, Spinger-Verlag: Berlin, **1973**.
[137] Wen, Z.; Zhao, M.; Jiang, Q. *J. Phys.: Condens. Matter*, **2000**, *12*, 8819 and all references therein.
[138] Jiang, Q.; Liang, L.H.; Zhao, M. M *J. Phys. Condens. Matter*, **2001**, *13*, L397 and references therein.
[139] Tsui, O.K.C.; Russell, T.P.; Hawker, C.J. *Macromolecules*, **2001**, *34*, 5535.
[140] http://fajerpc.magnet.fsu.edu/Education/2010/Lectrures/3_Chemical_Bonds.htm
[141] Couchman, P.R. *Macromolecules*, **1978**, *11*, 1156.
[142] Ao, Z.M.; Jiang, Q. *Langmuir*, **2006**, *22*, 1241 and references therein.
[143] Lang, X.Y.; Zheng, W.T.; Jiang, Q. *Phys. Rev. B*, **2006**, *73*, 224444 and references therein.
[144] *Periodic Table of the Elements*, Gaston: Oregon, **1993**, pp. 1.
[145] Weast, R.C. *CRC Handbook of Chemistry and Physics*, 69th ed., CRC Press: Boca Raton, FL, **1988-1989**, pp. E-125.
[146] Ishikawa, K.; Yoshikawa, K.; Okada, N. *Phys. Rev. B*, **1988**, *37*, 5852.
[147] Strukov, B.A.; Davitadze, S.T.; Kravchun, S.N.; Taraskin, S.A.; Goltzman, M.; Lemanov, V.V.; Shulman, S.G. *J. Phys.: Condens. Matter*, **2003**, *15*, 4331.
[148] Yu, T.; Shen, Z.X.; Toh, W.S.; Xue, J.M.; Wang, J. *J. Appl. Phys.*, **2003**, *94*, 618.
[149] Pogrebnyakov, A.V.; Redwing, J.M.; Jones, J.E.; Xi, X.X.; Xu, S.Y. Li, Q.; Vaithyanathan, V.; Schlom, D.G. *Appl. Phys. Lett.*, **2003**, *82*, 4319.
[150] Zhang, M.; Efremov, M.Yu.; Schiettekatte, F.; Olson, E.A.; Kwan, A.T.; Lai, S. L.; Wisleder, T.; Greene, J.E.; Allen, L.H. *Phys. Rev. B*, **2000**, *62*, 10548.
[151] Jiang, Q.; Yang, C.C.; Li, J.C. *Mater. Lett.*, **2002**, *56*, 1019.
[152] Sargent-Welch Scientific Company, *Table of Periodic Properties of the Elements*, Skokie: Illinois, **1980**, pp. 1-2.
[153] Massalski, T.B. *Binary Alloy Phase Diagrams, Metals Park*, American Society for Metals: OH, **1986**, Vol. *1*, pp. 942.
[154] Massalski, T.B. *Binary Alloy Phase Diagrams, Metals Park*, American Society for Metals: OH, **1986**, Vol. *2*, pp. 1248.
[155] Kim, S.S.; Sanders Jr, T.H. *J. Am. Ceram. Soc.*, **2001**, *84*, 1881.
[156] Wetmore, F.E.W.; Leroy, D.J. *Principles of Phase Equilibria*, 1st ed. McGraw-Hill Book Company, Inc.: Toronto, Canada, **1951**, pp. 76.
[157] http://webbook.nist.gov/chemistry
[158] Weast, R.C. *Handbook of Chemistry and Physics*, 69th ed., CRC Press: Boca Raton, FL, **1988-1989**, pp. C-667.
[159] Weast, R.C. *Handbook of Chemistry and Physics*, 69th ed., CRC Press: Boca Raton, FL, **1988-1989**, pp. B-193-195.
[160] Dean, J.A. *Lange's Handbook of Chemistry*, 13th Edition, McGraw-Hill Book Company: New York, **1985**, pp. 7-264.
[161] Sargent-Welch Scientific Company, *Periodic Table of the Elements*, Skokie: Illinois, **1979**, pp. 1.
[162] Saunders, N.; Miodownik, A.P.; Dinsdale, *CALPHAD*, **1988**, *12*, 351.
[163] Guillermet, A.F. *Z. Metallkd.*, **1991**, *82*, 478.
[164] Ubbelohde, A.R. *The Molten State of Matter*, John Wiley & Sons: New York, **1978**, pp. 241.
[165] Ubbelohde, A.R. *Melting and Crystal Structure*, Oxford Univ Press.: London, **1965**, pp. 171.
[166] Vinet, B.; Magnusson, L.; Fredriksson, H.; Desré, P.J. *J. Colloid Interface Sci.*, **2002**, *255*, 363.
[167] Borelius, G. in: *Solid State Physics*, Seitz, F. and Turnbull, Ed.; D. Academic

Press: New York, **1963**, pp. 1.
[168] Yavari, A.R. *Phys. Lett. A*, **1983**, *95*, 165.
[169] Boher, P.; Giron, F.; Houdy, P.; Beauvilain, P.; Chappert, C.; Veillet, P. *J. Appl. Phys.*, **1991**, *70*, 5507.
[170] Vavra, W.; Barlett, D.; Egaloz, S.; Uher, C.; Clarke, R. *Phys. Rev. B*, **1993**, *47*, 5500.
[171] Thompson, G.B.; Banerjee, R.; Fraser, H.L. *Appl. Phys. Lett.*, **2004**, *84*, 1082.
[172] Lowe, W.P.; Geballe, T.H. *Phys. Rev. B*, **1984**, *29*, 4961.
[173] Gruen, D.M., *Ann. Rev. Mater. Sci.*, **1999**, *29*, 211.
[174] Winter, N.W.; Ree, F.H. *J. Comput. Aided Mater. Des.*, **1998**, *5*, 279.
[175] Jiang, Q.; Chen, Z.P. *Carbon*, **2006**, *44*, 79.
[176] Sano, N.; Wang, H.; Alexandrou, I.; Chhowalla, M.; Teo, K.B.K.; Limura, K. *J. Appl. Phys.*, **2002**, *92*, 2783.
[177] Zazula, J.M. *On graphite transformations at high temperature and pressure induced by absorption of the LHC beam*, LHC Project Report 78/97: CERN, Geneva, **1997**.
[178] Fartaria, R.P.S.; Fernandes, F.M.S.S.; Freitas, F.F.M. *J. Phys. Chem. B*, **2002**, *106*, 10227.
[179] Okada, S.; Saito, S.; Oshiyama, A. *Phys. Rev. Lett.*, **1999**, *83*, 1986.
[180] Jing, X.; Chelikowsky, J.R. *Phys. Rev. B*, **1992**, *46*, 15503.
[181] Hwang, N.M.; Hahn, J.H.; Yoon, D.Y. *J. Cryst. Growth*, **1996**, *160*, 87.
[182] Hwang, N.M.; Hahn, J.H.; Yoon, D.Y. *J. Cryst. Growth*, **1996**, *160*, 55.
[183] Gamamik, M.Y. *Nanostruct. Mater.*, **1996**, *7*, 651.
[184] Chen, J.; Deng, S.Z.; Chen, J.; Yu, Z.X.; Xu, N.S.; *Appl. Phys. Lett.*, **1999,** *74*, 3651.
[185] Jiang, Q.; Zhang, S.H.; Li, J.C. *J. Phys. D: Appl. Phys.*, **2004**, *37*, 102.
[186] Horváth, J.; Birringer, R.; Gleiter, H. *Solid State Commun.*, **1987**, *62*, 319.
[187] Jiang, Q.; Zhang, S.H.; Li, J.C. *Solid State Commun.*, **2004**, *130*, 581.
[188] Yang, C.C.; Li, J.C.; Jiang, Q. *Solid State Commun.*, **2004**, *129*, 437.
[189] Yang, C.C.; Jiang, Q. *Scripta Mater.*, **2004**, *51*, 1081.
[190] Ma, L.-Y.; Tang, L.; Guan, Z.-L.; He, K.; An, K.; Ma, X.-C.; Jia, J.-F.; Xue, Q.-K. *Phys. Rev. Lett.*, **2006**, *97*, 266102.

Received: January 16, 2007 Revised: January 25, 2007 Accepted: June 21, 2007